Available online at www.sciencedirect.com

ScienceDirect

Advances in Space Research 76 (2025) 7390–7411

ADVANCES IN SPACE RESEARCH (a COSPAR publication)

www.elsevier.com/locate/asr

Ionospheric disturbances over the American sector during the May 2024 solar storm: flares and geomagnetic effects (May 9–15)

Ahmed Abdelaziz [a,b,c], Xiaodong Ren [c], Xuan Le [c], Chen Jinyuan [c], Dengkui Mei [c], Jinsheng Zhang [c], Xiaohong Zhang [a,c,d,*]

[a] State Key Laboratory of Information Engineering in Surveying, Mapping and Remote Sensing (LIESMARS), Wuhan University, 430079, China
[b] Civil Engineering Department, Benha Faculty of Engineering, Benha University, Benha 13511, Egypt
[c] School of Geodesy and Geomatics, Wuhan University, 430079, China
[d] Chinese Antarctic Center of Surveying and Mapping, Wuhan University, 430079, China

Received 16 May 2025; received in revised form 5 October 2025; accepted 6 October 2025
Available online 10 October 2025

Abstract

In May 2024, during a period of intense solar and geomagnetic activity, including the G5-class Gannon storm and X-class flares, we had a unique opportunity to study how these space weather events affected the ionospheric disturbance in low-to-mid latitude regions (40S to 40N) across America. This research examines the impacts of solar flares (SFs) and the Gannon storm on ionospheric electron density (Ne) and total electron content (TEC), utilizing data from the FORMOSAT-7/COSMIC-2 mission, ground-based ionosondes, and independent global TEC maps. Significant Ne enhancements were observed above 300 km, with Ne increasing by 137.7 % in the northern (0–40°N) and 129.2 % around 200 km in the southern (0–40°S) low-to-mid latitude regions during the storm peak, relative to quiet-time values on May 8 (DOY 129). Disk flares had a stronger impact on low-latitude regions, raising Ne by 28.66 % compared to mid-latitudes, while geomagnetic disturbances affected mid-latitudes more, with increases of 44.6 % during the storm's peak, defined by the minimum Dst value (–412 nT) on May 12. Moreover, the IROTI index, calculated as the product of the time-integrated Detrended TEC (IDTEC) and ROTI, was more effective than Detrended TEC (DTEC) and ROTI in differentiating the impacts of SFs and geomagnetic storms but less so during recovery. Our findings underscore the complex interactions between space weather events and the ionosphere, highlighting the need for improved models and the use of multiple indices (e.g., IROTI, DTEC, ROTI) to enhance the reliability and integrity of GNSS positioning by improving ionospheric corrections.

Keywords: Extreme geomagnetic storm; Ionosphere; Total electron content (TEC); Ionospheric Ne; GNSS; IROTI

1. Introduction

The ionosphere plays a critical role in space weather studies, particularly for global navigation satellite systems (GNSS), where ionospheric delays caused by changes over time and space can disrupt positioning accuracy. These delays are typically managed using numerical simulations or ionosphere-free techniques (He et al., 2022). Geomagnetic storms, caused by solar wind plasma interacting with Earth's magnetic field, strongly disturb the ionosphere, altering electron densities and causing GNSS errors that are difficult to model (Peng et al., 2021). Several studies have explored the effects of intense solar flares (SFs) and

* Corresponding author at: State Key Laboratory of Information Engineering in Surveying, Mapping and Remote Sensing (LIESMARS), Wuhan University, 430079, China.
E-mail address: xhzhang@sgg.whu.edu.cn (X. Zhang).

https://doi.org/10.1016/j.asr.2025.10.023

geomagnetic storms on ionospheric behavior (Qian et al., 2019), and others have tried to model the ionosphere during these disturbances (e.g., Abdelaziz et al., 2025).

There have been notable geomagnetic disruptions as solar activity has increased in the run-up to a new solar cycle. Following a pattern of major storms, which included events in April 2023 (e.g., Arslan Tariq et al., 2024) and March 2024 (Solar Cycle 25) (e.g., Pansong et al., 2025), as well as March 2015 and September 2017 (Solar Cycle 24) (e.g., Qian et al., 2019), the May 2024 G5-class geomagnetic storm caused notable ionospheric disruptions (e.g., Themens et al., 2024). Wang et al. (2023) observed that geomagnetic storms lead to variations in the rate of total electron content (TEC) index (ROTI) and GNSS phase scintillations, with peaks exceeding 0.5 TECU/min and 0.8, respectively. Their analysis, using both GNSS data and space-based observations from FORMOSAT-7/COSMIC-2 satellites, also revealed the rise of the F-layer during these storms and significant degradation in precise point positioning (PPP) accuracy at high latitudes.

The March 2015 St. Patrick's Day storm, classified as G4 by the National Oceanic and Atmospheric Administration (NOAA), has been extensively studied for its ionospheric effects. Morozova et al. (2020) employed principal component analysis on TEC data to extract empirical orthogonal functions, identifying correlations with solar ultraviolet (UV)/X-ray fluxes, solar wind parameters, and geomagnetic indices. Nava et al. (2016) examined ionospheric fluctuations across various regions and highlighted diverse phenomena caused by the storm. Zakharenkova et al. (2018) used GNSS and Swarm satellite data to detect large-scale plasma anomalies and highly structured auroral ionospheric regions spanning approximately 850 km.

Similarly, the September 2017 storm, driven by coronal mass ejections (CMEs), caused widespread ionospheric disturbances, disrupting GPS, radio communications, and other technologies that rely on the ionosphere (Alfonsi et al., 2021). Liu et al. (2019) analyzed GNSS data and SWARM observations during this storm, identifying medium-scale traveling ionospheric disturbances (MSTIDs) with variations exceeding 2.5 TECU. Alfonsi et al. (2021) noted a scattered distribution of electron density (Ne) in the Indian sector, highlighting the complex behavior of equatorial plasma bubbles (EPBs).

During the early phase of Solar Cycle 25, strong geomagnetic storms were rare but impactful. For example, the February 2022 SpaceX incident, caused by a geomagnetic storm, led to the failure of 38 Starlink satellites, which re-entered Earth's atmosphere (Hapgood et al., 2022). As Solar Cycle 25 approaches its peak, solar activity has surpassed that of Cycle 24, with increased solar flux (F10.7) and interplanetary magnetic field (IMF) intensity (Nagovitsyn and Ivanov, 2023). While geomagnetic storms predominantly affect high latitudes, this study focuses on low-to-mid latitudes to explore understudied regional responses and their implications for GNSS users in densely populated areas. For example, Dal Poz et al. (2025) highlighted the Gannon storm's effect on precise point positioning (PPP) at low-latitude regions in May 2024 over Brazil. They evaluated the three-dimensional positioning accuracy that had risen four times during the main phase of the storm compared to the previous day. High-latitude dynamics are well-documented (e.g., Foster, 1993; Themens et al., 2024), but the interplay of SFs and storms at lower latitudes remains less understood.

The G5-class Gannon storm, which occurred in May 2024, was one of the most intense geomagnetic storms in recent decades. Hajra et al. (2024) reported that a series of powerful CMEs and SFs drove the storm. The IMF and solar wind conditions during this period were characterized by an impulse amplitude of +88 nT, followed by a three-step storm main-phase development with SYM-H peaks of −183 nT, −354 nT, and −518 nT. The storm was driven by a powerful interplanetary shock and strong southward magnetic fields. These conditions led to significant geomagnetic disturbances, which had profound effects on the Earth's dynamic ionosphere.

Prior studies indicate that the ionospheric impact of SFs depends on their position on the solar disk (Mawad, 2024; Qian et al., 2012) and their rise and decay characteristics (Qian et al., 2019). Flares at the center of the Sun cause a significant increase in the Ne and TEC rather than those at the edges, due to their higher energy flux to Earth (Bruce T. Tsurutani et al., 2005). Disk flares face minimal absorption in the solar corona, delivering higher energy flux (Qian et al., 2011). The Halloween flares (2003) demonstrated this starkly: the X17.2 disk flare ($\theta = 8°$), where θ is the flare's angular distance from the disk center, caused 14.7 TECu enhancement, while the X28 limb flare ($\theta = 83°$) produced only 4.5 TECu despite a higher X-ray class (Liu et al., 2006). SFs can occur before, during, or after geomagnetic storms, making ionospheric behavior harder to predict (Qian et al., 2020). The Gannon storm in May 2024, preceded by three powerful X-class disk flares and followed by seven additional X-class flares, including an X8.7 flare—the strongest of Solar Cycle 25—needs more study to understand its effects on the ionosphere.

This study aims to investigate the complex interplay between solar and geomagnetic activities and their effects on ionospheric dynamics. The Data and Methodology section details the data sources and analysis approach, while Section 3 presents the findings and discusses the results in depth. The study concludes with a summary of key insights in Section 4.

2. Data and methodology

Typically, a CME or a high-speed solar wind stream takes between 1 and 3 days to travel from the Sun to Earth, depending on its velocity, leading to disturbances that can persist for an additional 3 to 4 days following the storm. Moreover, when an SF erupts on the solar disk, its effects reach Earth in several phases, such as solar energetic particles (SEPs) and CMEs. Following Villaverde's approach

(Collado-Villaverde et al., 2024), this study focused on a period starting two days before the geomagnetic storm and extending to four days afterward, allowing time for recovery to normal conditions.

From May 8–15, 2024, Earth experienced a series of intense SFs and one of the strongest geomagnetic storms of Solar Cycle 25. The flares originated from active sunspot region 13664, with ten major events (X1.0 to X8.7 class) erupting across the sun's disk (Table 1). The flares (X5.89 and X1.5 on May 11 and X1.02 on May 12) occurred near the Sun's western limb, while other powerful flares were more centrally positioned—critical for Earth-directed impacts.

The storm's severity became clear through multiple indicators:

- Solar wind speeds (Fig. 1c) surged from ~400 km/s to over 800 km/s during the storm's peak day, carrying enhanced energy toward Earth.
- The IMF Bz component (Fig. 1b) turned sharply southward (−46.5 nT), enabling efficient energy transfer into our magnetosphere (Tsurutani et al., 2008).
- Kp index values hit 9 (the maximum scale), while SYM-H/Dst (Fig. 1a) recorded three distinct drops to −518 nT—a hallmark of extreme ring current strengthening (Hajra et al., 2024).

This wasn't just a textbook storm. The IMF By component's unusual spike (+63.4 nT) introduced hemispheric asymmetries in auroral activity, while the combined solar wind pressure and Bz conditions created perfect conditions for global ionospheric disturbances. The storm's main phase began abruptly at 22:54 UT on May 10 (green dashed line in Fig. 1), coinciding with a steep SYM-H and Dst decline, extreme solar wind velocities, and sustained negative Bz.

These factors collectively triggered the ionospheric perturbations we analyze later (Figs. 3–12), including traveling atmospheric disturbances (TADs) that propagated from auroral to equatorial latitudes (Fuller-Rowell & Codrescu, 1994). The event underscores how solar wind dynamics—not just flare intensity—dictate geomagnetic impacts. This mechanism helps explain the low-latitude ionospheric perturbations observed in subsequent sections.

2.1. Electron density datasets (COSMIC-2 & IONOSONDE)

Ionospheric electron density profiles (EDP) were analyzed to assess the impact of SFs and the Gannon storm on the ionosphere, utilizing level 2 data of the COSMIC-2 mission and ground-based ionosonde measurements. The COSMIC-2 data, covering the American sector from May 8 to 15, was used to observe ionospheric behavior in low- to mid-latitude regions across both hemispheres. Fig. 2b represents the ionospheric EDP structure from COSMIC-2 observation data at 06:17 LT on May 8, 2024, after rigorous quality control.

To further investigate Ne variation with altitude, two ionosonde stations were selected: Austin, USA (AU930) at (30.4°N, 97.7°W; dip latitude 39.5°N), and Cachoeira Paulista, Brazil (CAJ2M) at (22.7°S, 45°W; dip latitude 19.2°S), both of which had simultaneous measurements available, as represented by green stars in Fig. 2a.

EDPs from the Global Ionospheric Radio Observatory (GIRO) database (Reinisch and Galkin, 2011) were used in their entirety, including both measured bottom-side and modeled top-side portions. While SAOExplorer provides complete profiles for continuity, we note that the top-side reconstruction method is proprietary to the Digital Ionogram Database (DIDBase) system. These profiles are generated through:

1. Empirical extension above hmF2 using undisclosed algorithms that may incorporate historical patterns and/or IRI-class models.
2. Anchoring to the measured NmF2 and hmF2 from ionograms.

Only the bottom-side electron density values (≤hmF2), which are measured directly from ionograms, were included in statistical analyses. The top-side portion (>hmF2) is modeled by SAOExplorer and used here solely to provide qualitative context in Figs. 6–7. Where avail-

Table 1
The top 10 solar flares from sunspot region 13,664 between 8 and 15 May 2024.

Date	Start	Maximum	End	Location	Intensity	Limb/Disk flare	Rank
5/14/2024	16:46	16:51	17:02	S19W0	X8.79	Disk	1
5/11/2024	1:10	1:23	1:39	S18W67	X5.89	Limb	2
5/10/2024	6:27	6:54	7:06	S17W48	X3.98	Disk	3
5/15/2024	8:18	8:37	8:52	S19W0	X3.48	Disk	4
5/9/2024	8:45	9:13	9:36	S20W32	X2.2	Disk	5
5/14/2024	2:03	2:09	2:19	S19W0	X1.72	Disk	6
5/11/2024	11:15	11:44	12:05	S18W67	X1.5	Limb	7
5/14/2024	12:40	12:55	13:05	S19W0	X1.2	Disk	8
5/9/2024	17:23	17:44	18:01	S20W32	X1.1	Disk	9
5/12/2024	16:11	16:26	16:38	S18W73	X1.02	Limb	10

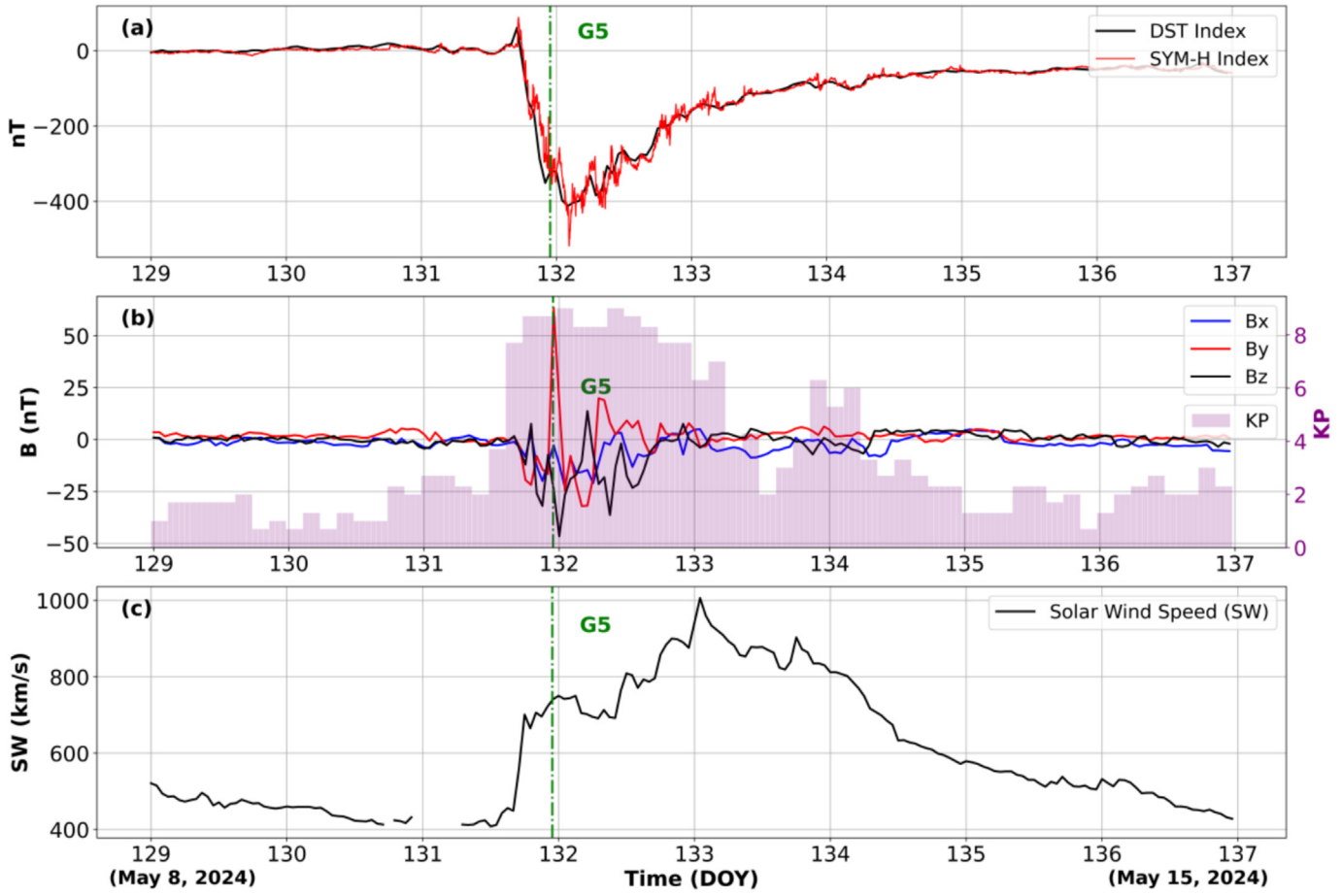

Fig. 1. Temporal evolution of geomagnetic and solar wind parameters during May 8–15, 2024, Gannon storm. (a) DST (black) and SYM-H (red) indices showing the storm's intensity in nT. (b) Interplanetary magnetic field components Bx (blue), By (red), and Bz (black) in nT, with Kp index (purple bars) overlaid. (c) Solar wind speed (black) in km/s. The vertical dashed green line marks the main phase of the G5-class geomagnetic storm at DOY 131.94 (May 10, 22:54 UT). All panels share the same time axis on Day of Year (DOY).

able, concurrent COSMIC-2 profiles were used to verify general morphological agreement.

There are potential uncertainties in retrieved Ne profiles, particularly those arising from Abel inversion assumptions, signal irregularities, and equatorial anomaly conditions. Furthermore, spaceborne observations can be influenced by equipment failure or intense solar-terrestrial events; therefore, it is critical to check RO profiles for quality control. The following checks were performed to avoid noisy and erratic profiles: First, profiles having negative values at altitudes of 100 km or above are excluded. Additionally, hmF2 values outside the 200–450 km range are excluded (Abdelaziz et al., 2025). Following data quality assessment, we chose Ne profiles at F-layer heights ranging from 150 km to 550 km, with profiles recorded approximately every 1.5 min.

2.2. GNSS datasets (IGS & RBMC) and ionospheric TEC indices

As of May 15, 2024, the International GNSS Service (IGS) has established 522 GNSS stations globally, providing extensive raw observational data crucial for geophysical and space physics research. Additionally, the Brazilian Network for Continuous Monitoring of GNSS Systems (RBMC) consists of 120 continuously operating GNSS reference stations across Brazil. For this study, we selected 30 IGS stations and 37 RBMC stations. Slant TEC (STEC) is defined as the integral of Ne along the Line of Sight (LoS) between the satellite and receiver (Ciraolo et al., 2007). The ionospheric STEC was calculated using a carrier phase smoothing pseudorange approach based on dual-frequency data from these GNSS stations, recorded at a 30-second sampling rate from May 8 to 15, 2024.

$$\mathrm{STEC} = \frac{\mathrm{I}^{s}_{r,0}.\mathrm{f}_0^2}{40.31 \times 10^{16}} = \frac{-\tilde{\mathrm{L}}\,\mathrm{r},4s + \left(\lambda_1 \mathrm{N}^{s}_{r,1} - \lambda_2 \mathrm{N}^{s}_{r,2}\right) + \varepsilon^{s}_{r}.\mathrm{f}_0^2}{40.31 \times 10^{16}.(\gamma_1 - \gamma_2)} \quad (1)$$

where $\tilde{\mathrm{L}}\,\mathrm{r},4s$ represents a geometry-free combination of phase observations; λ_1 and λ_2 ; are the wavelengths for f_1

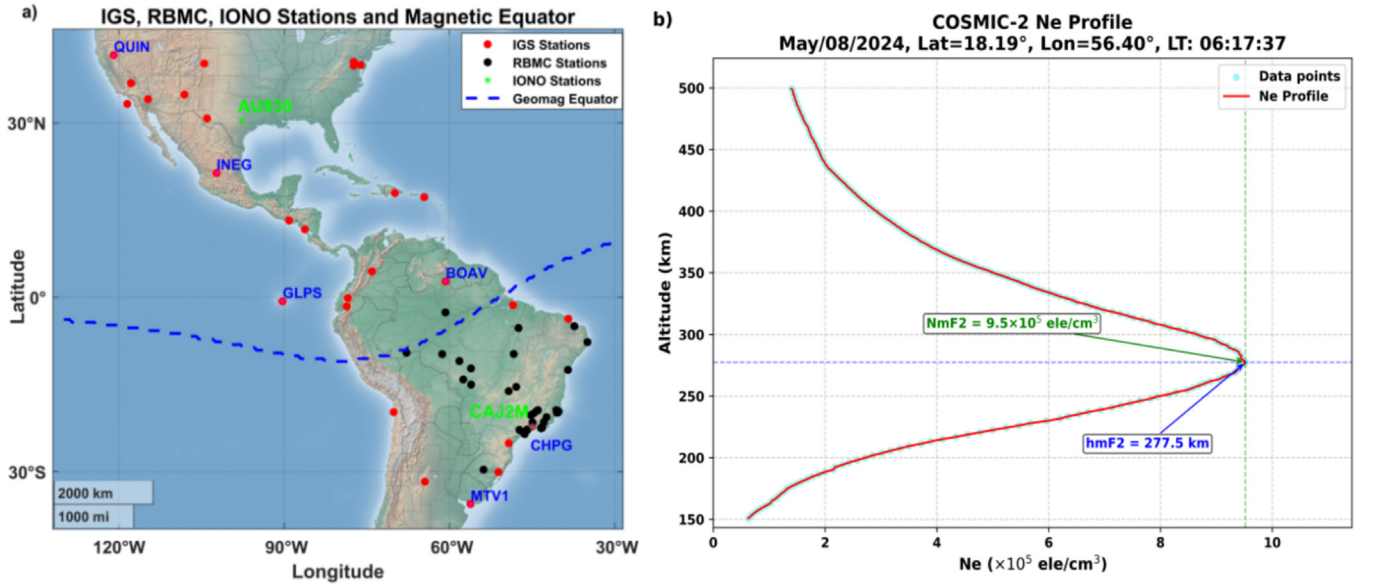

Fig. 2. (a) Observational network across the American sector: Distribution of GNSS stations (red = IGS, black = RBMC) and ionosonde locations (green stars) over low-to-mid latitudes, with the geomagnetic equator highlighted (blue dashed line). (b) Ionospheric electron density profile (EDP): COSMIC-2-derived vertical structure on 8 May 2024 after rigorous quality control.

and f_2, respectively; $N^s_{r,1}$ and $N^s_{r,2}$ refers to the carrier phase ambiguity for both frequencies; $\gamma_i = (f_0/f_i)^2$ is a scale factor, where$f_0 = 10.23$ MHZ. The STEC value is often stated in units of TECU (1 TECU = 10^{16} ele/m^2). The geometry-free phase combination cannot distinguish between ionospheric delay and carrier phase ambiguity, although noise (ε^s_r) can be disregarded. However, the carrier phase ambiguity remains consistent across different frequencies in successive time epochs. Consequently, the TurboEdit algorithm is employed for cycle slip detection during data preprocessing, as described by Blewitt (2008).

Pi et al. (1997) proposed the use of the rate of TEC (ROT) and ROTI as metrics for detecting ionospheric anomalies over short time intervals, effectively eliminating diurnal and seasonal variations. ROT represents the time derivative of STEC values between two consecutive time epochs and can be calculated as follows:

$$ROT = \frac{STEC^p_i - STEC^p_{i-1}}{t_i - t_{i-1}} \quad (2)$$

where t_i represent an epoch time and p is the serial number of a satellite. The ROT value is an accurate measure of the ionospheric TEC along LoS due to fluctuating phases and is often expressed in TECU per minute (TECU/min). Because ROT frequently swings around a low value, Pi et al. (1997) developed the ROTI to identify and statistically depict smaller-scale irregularities:

$$ROTI = \sqrt{\langle ROT^2 \rangle - \langle ROT \rangle^2} \quad (3)$$

where the angle bracket indicates the average over 5 min time window.

Another way to eliminate diurnal and seasonal trends, Saito et al. (1998) introduced the moving average method to detrend TEC, which is known as Detrended TEC (DTEC):

$$DTEC(i) = STEC(i) - \frac{1}{N}\sum_{j=i-N/2}^{j=i+N/2} STEC(j) \quad (4)$$

where STEC(i) and STEC(j) are the STEC value at time i and j; N is set to 60 representing the moving average window width in 30 min as the utilizing data sampled at 30 s intervals. The time range is set to [i−N/2, i+N/2].

However, moving average detrending can introduce artifacts, particularly for longer-period variations (20–60 min), which may distort wave signatures in TEC data and affect automated processing or TID detection (Maletckii et al., 2020). Maletckii et al. (2020) analyzed various detrending and variation selection methods, finding that the centered moving average filter performs best among the tested methods (e.g., Butterworth, Chebyshev filters). In this study, we use a 30-min moving average for DTEC calculation to balance sensitivity to short-term perturbations with computational efficiency, consistent with prior GNSS studies (Saito et al., 1998). To mitigate potential artifacts, we cross-validate DTEC results with COSMIC-2 radio occultation profiles and ionosonde measurements, ensuring robust detection of ionospheric disturbances.

Ren et al. (2024) found that ROTI tends to remain low during the occurrence of TIDs in low-to-mid latitude regions, likely due to the dominance of MSTIDs driven by atmospheric gravity waves or geomagnetic storm effects, which produce fewer small-scale irregularities compared to

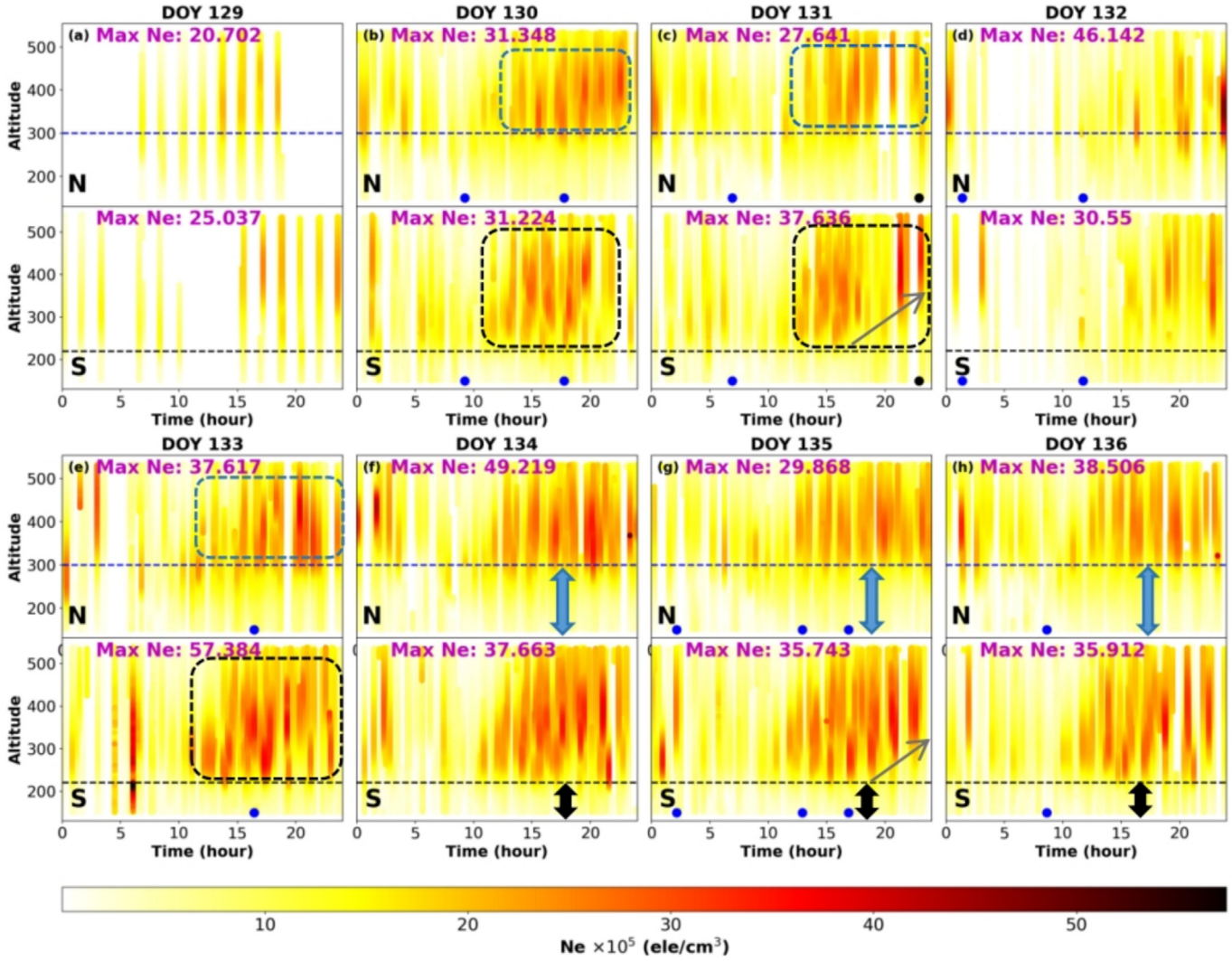

Fig. 3. 24-h electron density distribution from COSMIC-2 data, covering altitudes between 150 km and 550 km, spanning longitudes from 30°W to 130°W, for days DOY 129 to DOY 136 (May 8–15, 2024). The data shows Ne variations in both the northern (N) and southern (S) regions over the American sector, with the maximum Ne for each day indicated in purple. Blue dotted lines highlight altitudes around 300 km, black dotted lines represent altitudes around 220 km, blue dots represent the SFs time, and the black dot represents the Gannon storm main phase.

auroral regions (Ren et al., 2024), making TIDs challenging to detect, especially during quiet periods or when they are isolated outliers. To address this, they calculated the integral of DTEC (IDTEC) over time for discrete DTEC values:

$$\mathrm{IDTEC} = \sum_{i=1}^{n} |\mathrm{DTEC}(i)| \cdot \Delta t \tag{5}$$

where |DTEC(i)| is the absolute value of the DTEC at time (i); Δt is the time interval of discrete DTEC; n is the number of DTEC within 5 min. The IDTEC is often expressed in units of TECU · min.

By gathering the time integral IDTEC and ROTI, they expressed this coupling by IROTI:

$$\mathrm{IROTI} = \mathrm{IDTEC} \cdot \mathrm{ROTI} \tag{6}$$

where the IROTI value is typically expressed in units of TECU^2.

3. Results and discussion

This study focused on the ionospheric response in both the Northern and Southern Hemisphere of the American sector, with data covering latitudes from 40°N to 40°S and longitudes from 30°W to 130°W. This ensures that both hemispheres of the American sector are sufficiently represented, allowing for a comparative analysis of their ionospheric behavior.

The ionospheric response to geomagnetic storms is governed by a series of complex physical processes, as described by Prölss (1995) and Schunk and Nagy (2009). These processes lead to significant changes, including alterations in thermospheric composition and ionization depletion at middle latitudes. These phenomena are critical to understanding the ionospheric disturbances observed during the G5 Gannon storm. For instance, the depletion of ionization at mid-latitudes can lead to significant reduc-

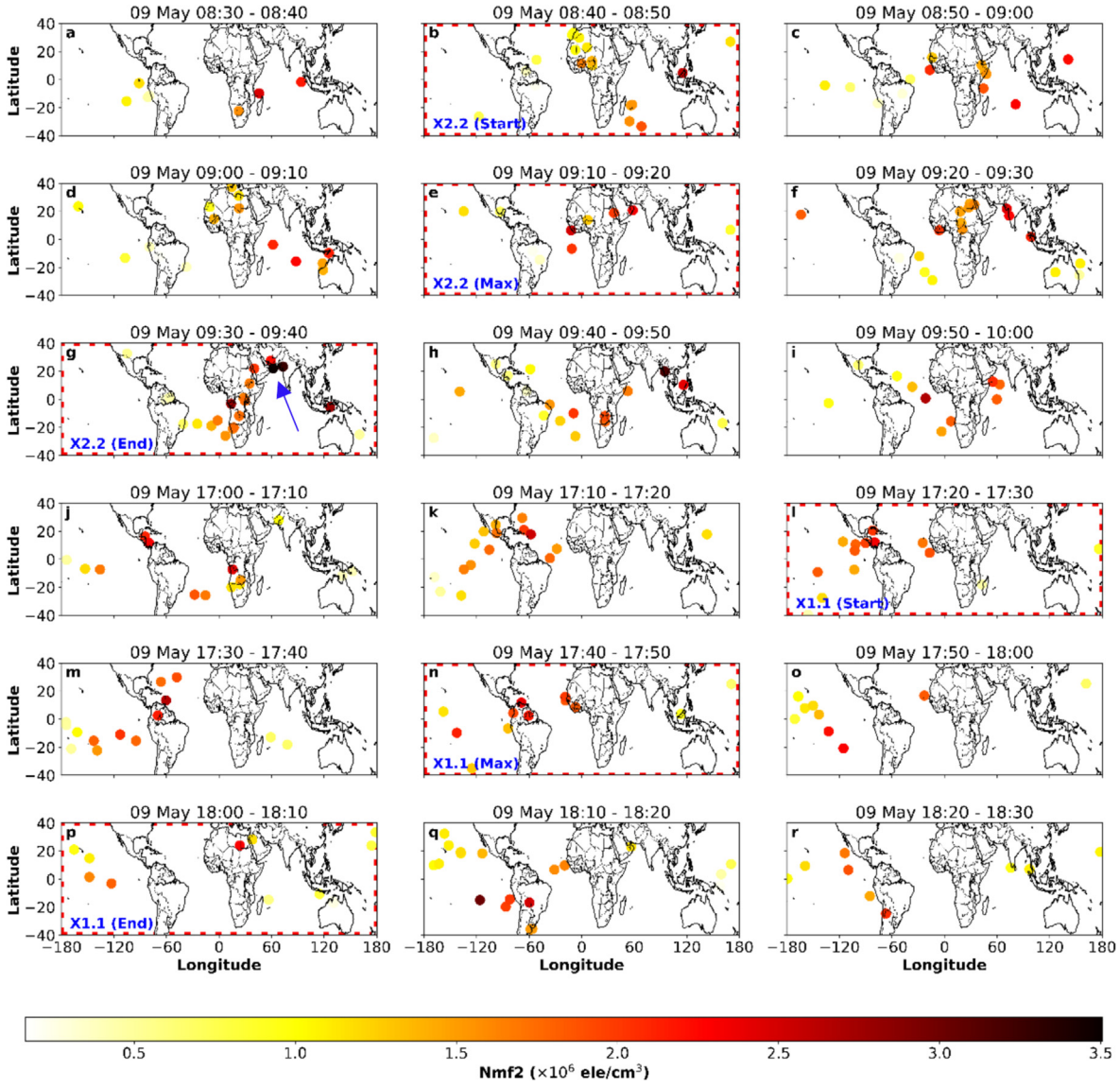

Fig. 4. Global spatial and temporal NmF2 Distribution on DOY 130, 2024: Panels (a–i) show ionospheric electron density from 08:30 to 10:00 UT during the X2.2 solar flare event, and panels (j–r) from 17:00 to 18:30 UT during the X1.1 solar flare event, with a unified color scale (×10^6 ele/cm^3). Blue text indicates the intensity and phase of the solar flares (start, maximum, end), while red dotted boxes highlight their time intervals.

tions in TEC, while the displacement of the EIA crests can cause localized enhancements in TEC at low latitudes.

In this study, such EIA crest displacements are not measured directly, as evidenced by low-latitude effects including auroral observations in regions like Mexico (Gonzalez-Esparza et al., 2024); instead, they are inferred from indirect signatures in the IROTI maps and ΔTEC time series (Figs. 8, 9, and 11), including mid-latitude TEC depletion and hemispheric asymmetry in Ne disturbances (Fig. 3), which are consistent with PPEF (prompt penetration electric field)-driven latitudinal shifts reported in previous studies (Astafyeva et al., 2025; Danilchuk et al., 2025).

Astafyeva et al. (2025) further highlight electrodynamic puzzles during the May 2024 superstorm, including enhanced super-fountain effects and asymmetric ionospheric responses, which align with our observed hemispheric differences in Ne and TEC depletions. Additionally, Danilchuk et al. (2025) reported transient intersections of the auroral oval and EIA crest over the American sector during the May 2024 storm, but such events are highly variable and dependent on localized geophysical conditions. These processes must be considered when analyzing the ionospheric response to geomagnetic storms, as they can significantly impact satellite signals passing through the ionosphere.

3.1. Altitudinal electron density changes over low latitude regions

Our analysis emphasizes the ten most significant SFs during 8–15 May 2024, both before and following the

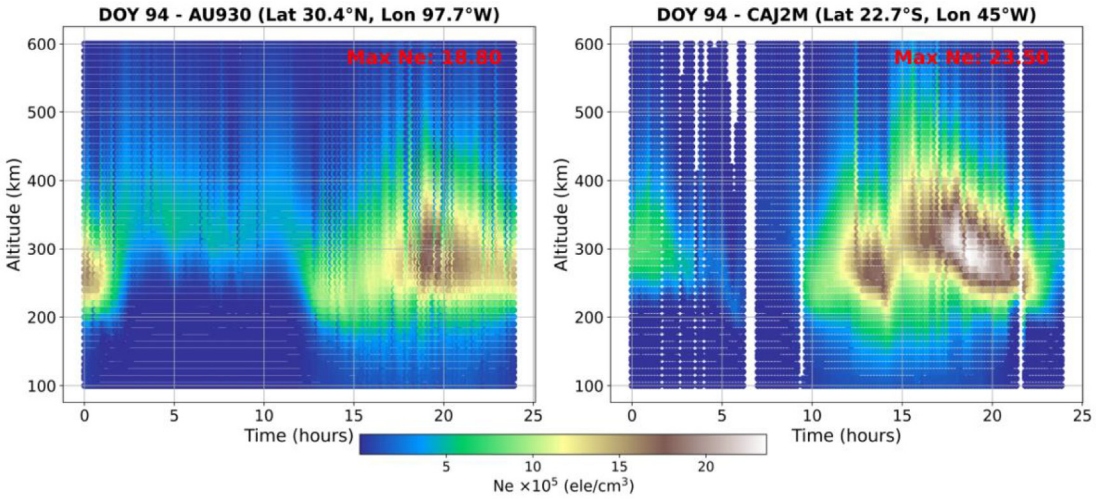

Fig. 5. Electron density distribution at the AU930 (30.4N, 97.7W; dip latitude 39.5N) and CAJ2M (22.7S, 45W; dip latitude 19.2S) stations during quiet DOY 94 (April 3, 2024).

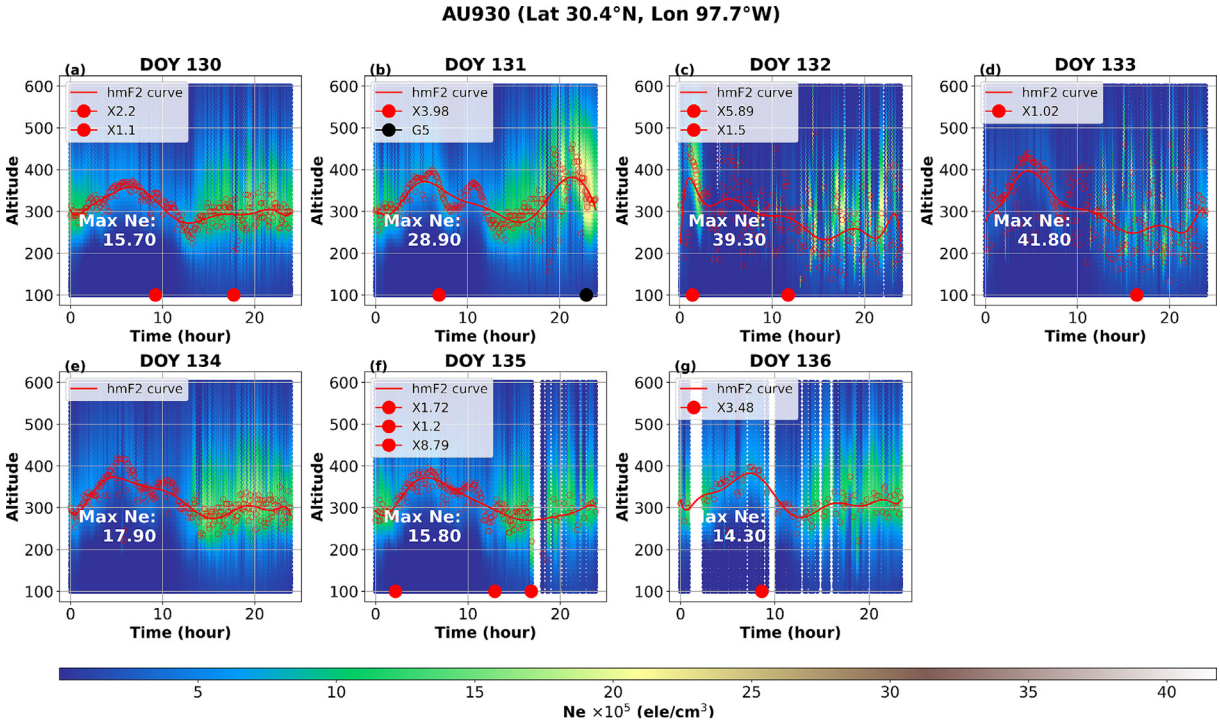

Fig. 6. Electron density variations measured by the Austin ionosonde station (30.4° N, 97.7° W; dip latitude 39.5° N) over seven consecutive days (DOYs 130–136, 2024). Panels (a)–(g) correspond to individual days. Red dots indicate the occurrence times of the ten most intense solar flares during this period, and the black dot marks the main phase of the G5 Gannon storm. Circle markers show the measured hmF2 for each profile, with the best-fit curve representing the hmF2 trend, above which electron density values are modelled rather than measured.

super-intense G5 Gannon storm, which first peaked at 22:54 UT on DOY 131. During this event, the By component reached approximately 63.4 nT, while the Bz component exhibited a strongly southward orientation at −24 nT. These conditions contributed to heightened auroral activity and enhanced ionospheric currents. In particular, prompt penetration electric fields (PPEFs) are known to displace the EIA crests toward higher latitudes. In our case, this displacement is inferred from GNSS and COSMIC-2 observations rather than direct crest tracking, based on characteristic spatial patterns of TEC enhancement at lower latitudes and depletion at mid-latitudes during the storm's main phase.

During the G5-class Gannon storm on DOY 132 (May 11), Ne exhibited notable variability across altitudes and hemispheres, expressed in units of ele/cm^3 (electrons per cubic centimeter). Peak disturbances were observed between 300 and 450 km, with Ne reaching

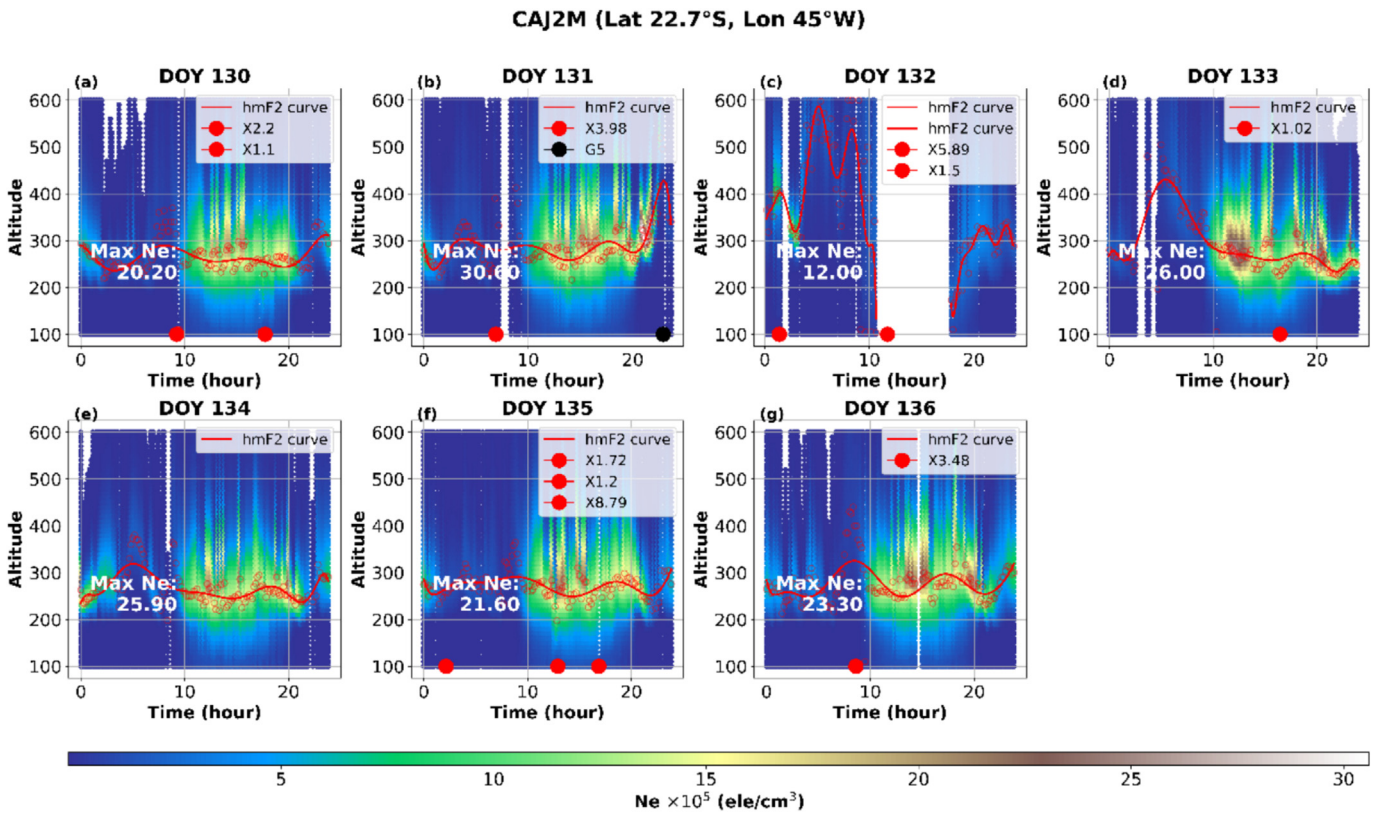

Fig. 7. Electron density variations measured by the Cachoeira Paulista ionosonde station (22.7°S, 45°W; dip latitude 19.2°S) over seven consecutive days (DOYs 130–136, 2024). Panels (a)–(g) correspond to individual days. Red dots indicate the occurrence times of the ten most intense solar flares during this period, and the black dot marks the main phase of the G5 Gannon storm. Circle markers show the measured hmF2 for each profile, with the best-fit curve representing the hmF2 trend, above which electron density values are modeled rather than measured.

4.61×10^6 ele/cm^3 in the north (a 52.2 % increase from DOY 129) and 3.06×10^6 ele/cm^3 in the south (Fig. 3a–d). Interestingly, the southern region showed an 18.6 % decrease relative to its peak on DOY 130, illustrating strong hemispheric asymmetry. This asymmetry was likely driven by the southward displacement of the geomagnetic equator and differences in thermospheric winds (Tsurutani et al., 2005, 2008).

The storm's main phase at 22:54 UT on DOY 131, marked by Bz dropping to −46.5 nT and SYM-H plunging to −354 nT, triggered a Ne rise within 1 h, especially at mid-latitudes. This rapid ionospheric response suggests PPEFs and neutral wind uplift as key mechanisms (Astafyeva et al., 2025; Besliu-Ionescu et al., 2022). Our findings of asymmetric Ne enhancements (e.g., 52.2 % in the north vs. 18.6 % decrease in the south) corroborate the electrodynamic forcing and super-fountain effects described by Astafyeva et al. (2025) for the May 2024 storm, particularly in low-to-mid latitudes. The dotted rectangles in Fig. 3 confirm these altitudinal responses, showing post-sunset enhancements consistent with enhanced plasma fountain effects.

On DOY 133, the electron density (Ne) in the southern hemisphere surged sharply to 5.74×10^6 ele/cm^3 at an altitude of 220 km, marking a 44.6 % increase from the previous day. This spike indicates a delayed storm recovery phase, likely amplified by sustained high-speed solar wind, as noted by Besliu-Ionescu et al. (2022). On DOY 134, while no severe solar flares occurred, coronal mass ejections (CMEs) drove an increase in Ne in the northern hemisphere, reaching 4.10×10^6 ele/cm^3 at 440 km between 2:00 and 3:00 UT. This was followed by a gradual decline, with Ne peaking again at 4.92×10^6 ele/cm^3 at 370 km by 23:00 UT (Fig. 3f). In contrast, disturbances in the southern hemisphere on DOY 134 were less pronounced than those on DOY 133, underscoring the asymmetric impacts alternating between hemispheres during storm days. These variations were shaped by a combination of magnetic field geometry, seasonal effects, atmospheric dynamics, geomagnetic storms, and solar wind influences.

Three disk SFs were observed by DOY 135, including the most intense flare of Solar Cycle 25 (X8.79). Despite these events, the Ne in the northern hemisphere gradually returned to pre-storm levels (~2.99×10^6 ele/cm^3), whereas in the southern hemisphere, the X8.79 flare sustained elevated Ne at ~3.57×10^6 ele/cm^3. Additionally, a discernible increase in hmF2 was observed (indicated by the gray arrow in Fig. 3g). This phenomenon arose as a secondary effect of the post-flare activity and associated CME, which generated propagating atmospheric gravity waves

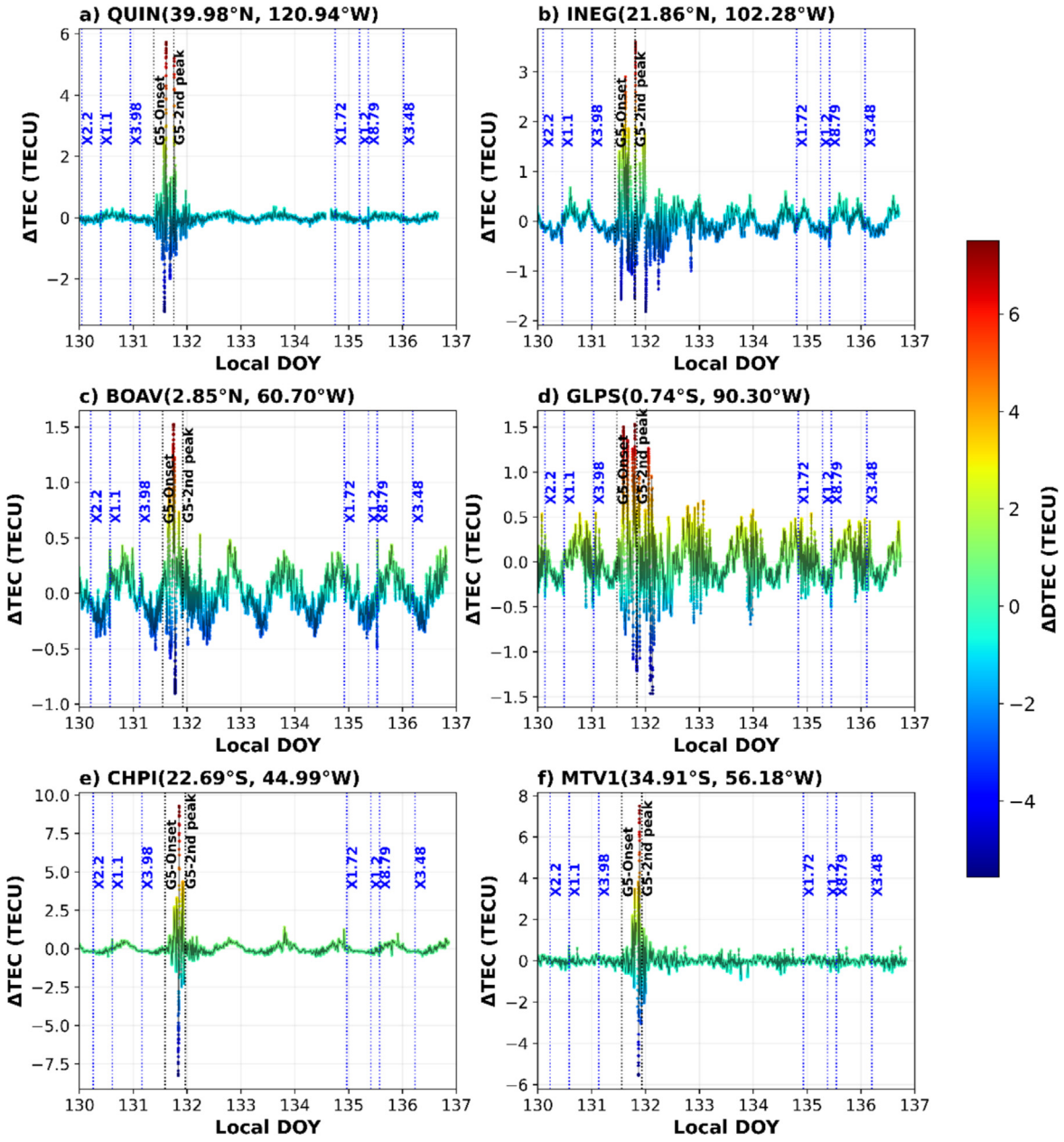

Fig. 8. TEC deviations (ΔTEC) from quiet-time baselines (average TEC of DOYs 115, 116, 142, 143) during disturbed days (DOYs 130–136, 2024) at six IGS stations in the Northern and Southern hemispheres of the American sector. Panels (a) and (f) show mid-latitude stations (QUIN, MTV1), (b) and (e) show low-latitude stations (CHPI, INEG), and (c) and (d) show equatorial stations (GLPS, BOAV).

(AGWs). These waves induced delayed hmF2 oscillations (Qian et al., 2012). The observed hmF2 enhancement at low latitudes can be attributed to increased X-ray and extreme ultraviolet (EUV) radiation, which enhanced ionization over recombination in the upper ionospheric layers (Song et al., 2022). Post-storm recovery extended over three days, with Ne gradually declining 38–50 % back toward pre-storm levels.

Overall, the Gannon storm and subsequent SFs had minimal ionospheric effects below 300 km in the north but significantly impacted altitudes down to 220 km in the south. COSMIC-2 Ne data revealed pronounced disturbances during the storm's peak, transitioning to minor storm conditions in subsequent days. Regarding the differences in ionospheric responses at various altitudes between the northern and southern hemispheres in the American sector during the storm, we suppose that this is highly likely related to the southward displacement of the geomagnetic equator. The southward shift of the geomagnetic equator causes the equatorial plasma fountain effect to move southward overall, resulting in varying degrees of upward ion drift at the same latitude in the low-latitude

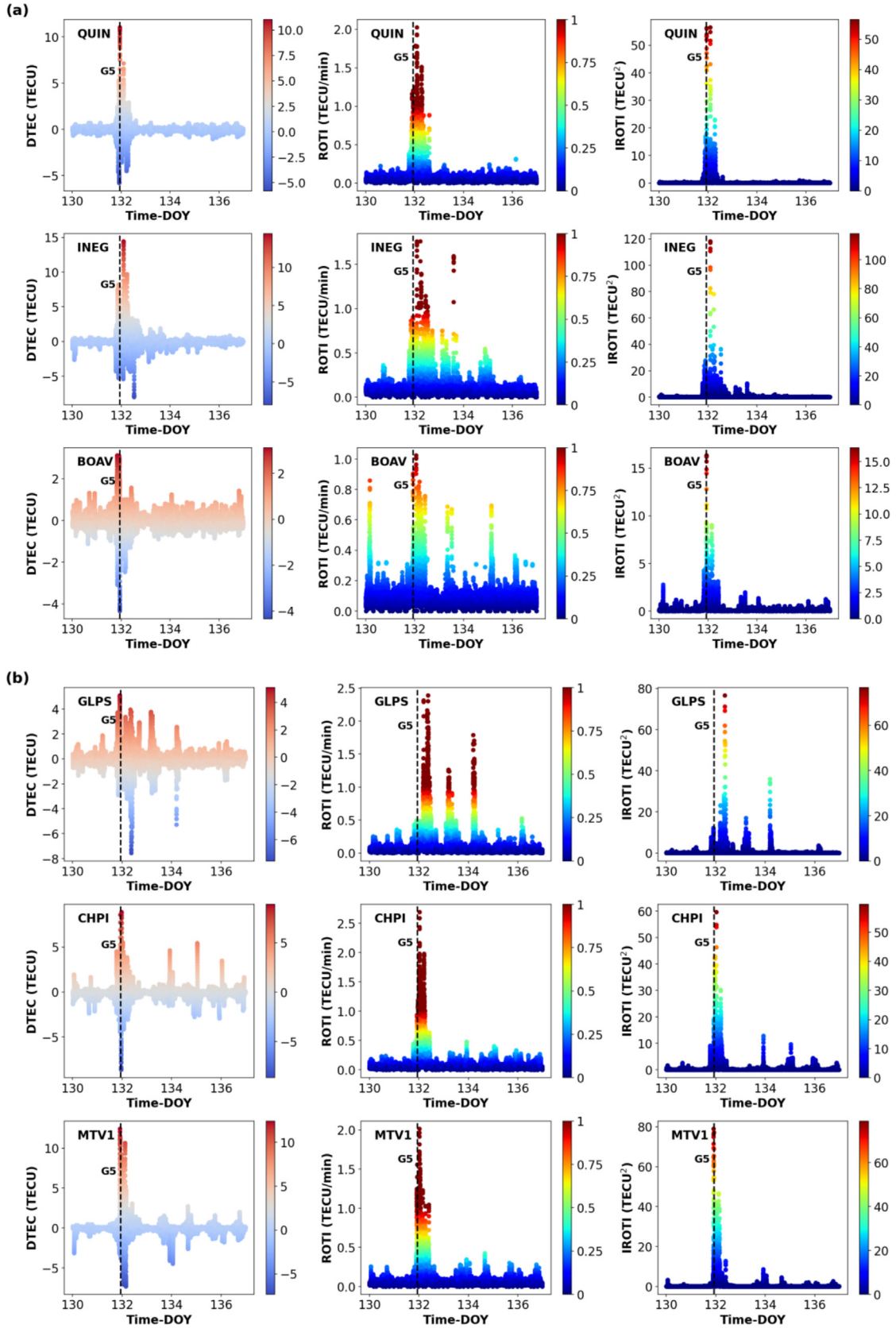

Fig. 9. (a): Displays the DTEC, ROTI, and IROTI metrics for three IGS stations in the Northern region, arranged by latitude from high to low. (b): Presents the DTEC, ROTI, and IROTI metrics for three IGS stations in the Southern region, similarly arranged by latitude from high to low.

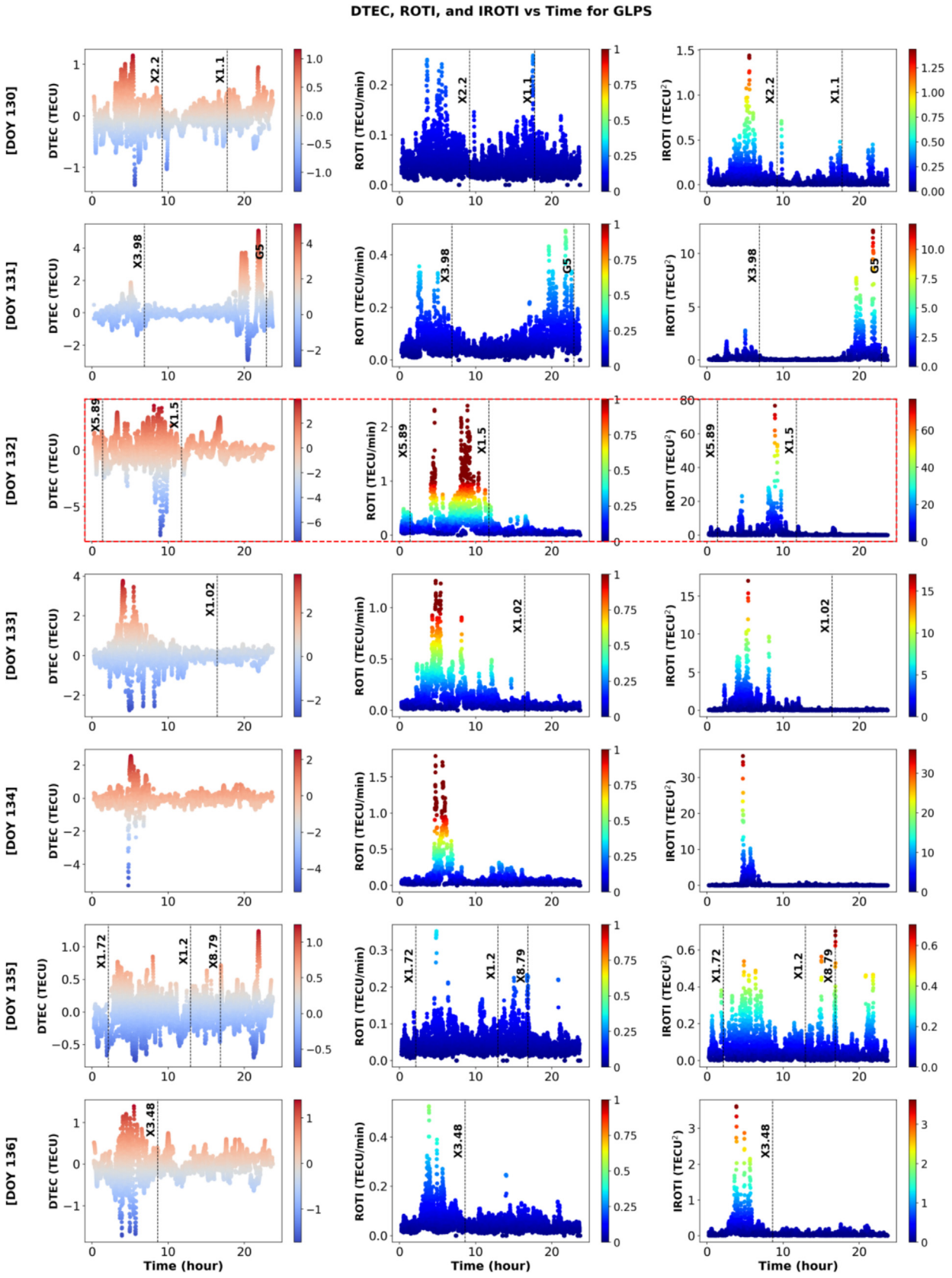

Fig. 10. Temporal profiles of DTEC, ROTI, and IROTI at six IGS stations in the American sector (40°S to 40°N) during the May 2024 G5-class Gannon storm (DOYs 130–136). Columns show DTEC (TECU), ROTI (TECU/min), and IROTI ($TECU^2$), respectively, with rows corresponding to each DOY.

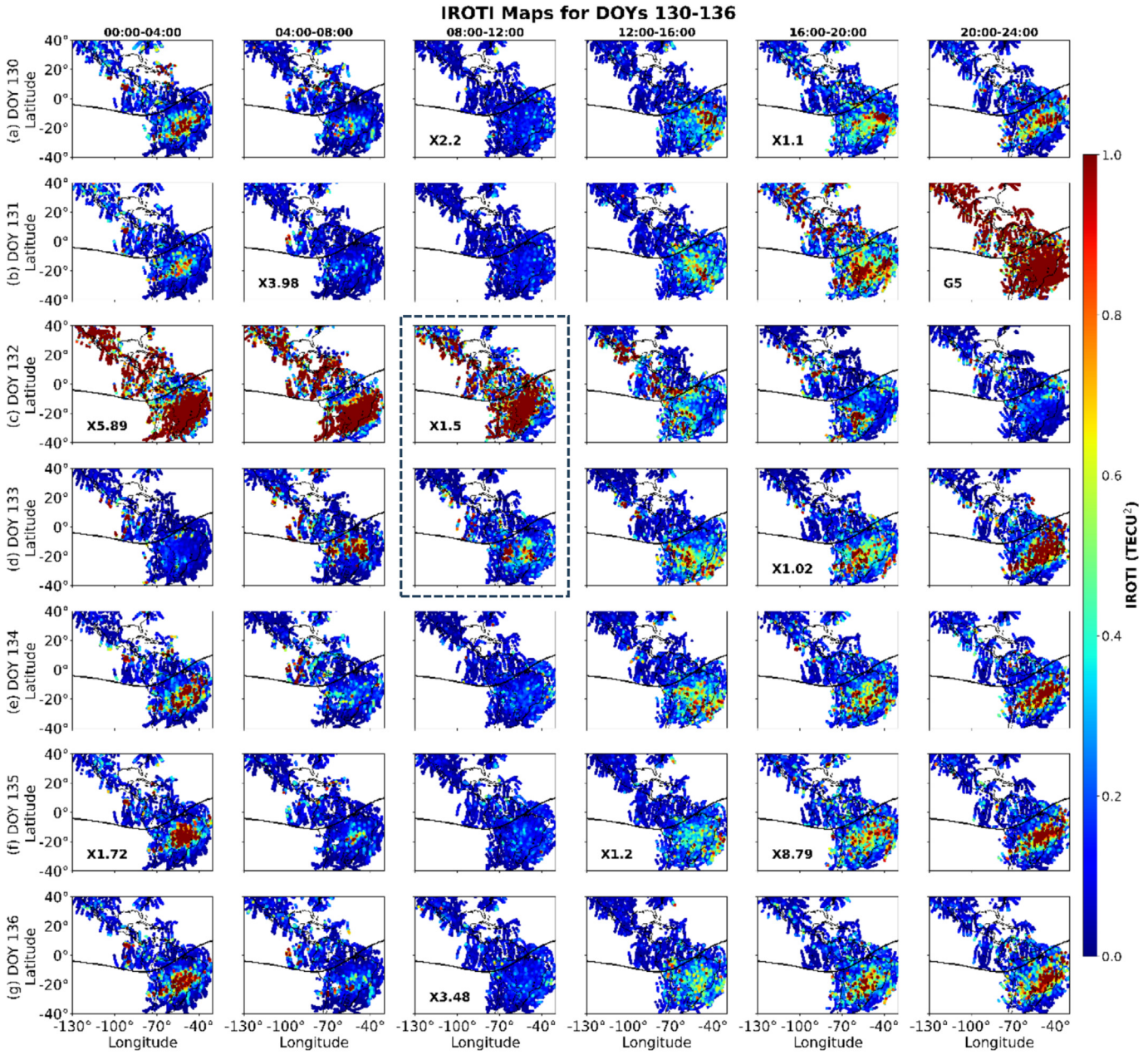

Fig. 11. Spatial and temporal distribution of IROTI across the American sector for DOY 130 to DOY 136, with data presented in 4-h intervals. The letters 'a' to 'g' correspond to DOYs 130 to 136, respectively. Text indicates the intensity of solar flares and geomagnetic storms, each annotated within its respective time frame. Black solid line represents the magnetic equator. And black dotted box highlights the time interval 8:00–12:00 in DOY 132 and 133.

regions of both hemispheres, with the ion accumulation zone in the northern hemisphere being generally higher than in the southern hemisphere.

3.2. Solar flare-induced enhancements in NmF2 across low latitudes

To investigate the impact of SFs on the equatorial ionospheric electron density, we analyzed global NmF2 distributions using COSMIC-2 observations across low-latitude regions, due to the lack of profile numbers that cover the American region within 10 min. Fig. 4 presents these variations at a 10-min window temporal resolution to capture spatiotemporal characteristics and rapid ionospheric responses.

The X2.2-class flare (Table 1) caused a significant increase in NmF2, especially over Oman between 09:30 and 09:40 UT (13:30–13:40 LT), as shown by the black-red dot and blue arrow in Fig. 4g. This sharp rise indicates that the flare's X-ray/EUV emissions directly ionized the area, which matches earlier research on how flares boost plasma density (e.g., Li et al., 2025; Saharan et al., 2023). Importantly, there was no major disturbance noted in the American region (08:30–10:00 UT / 05:30–07:00 Brazil

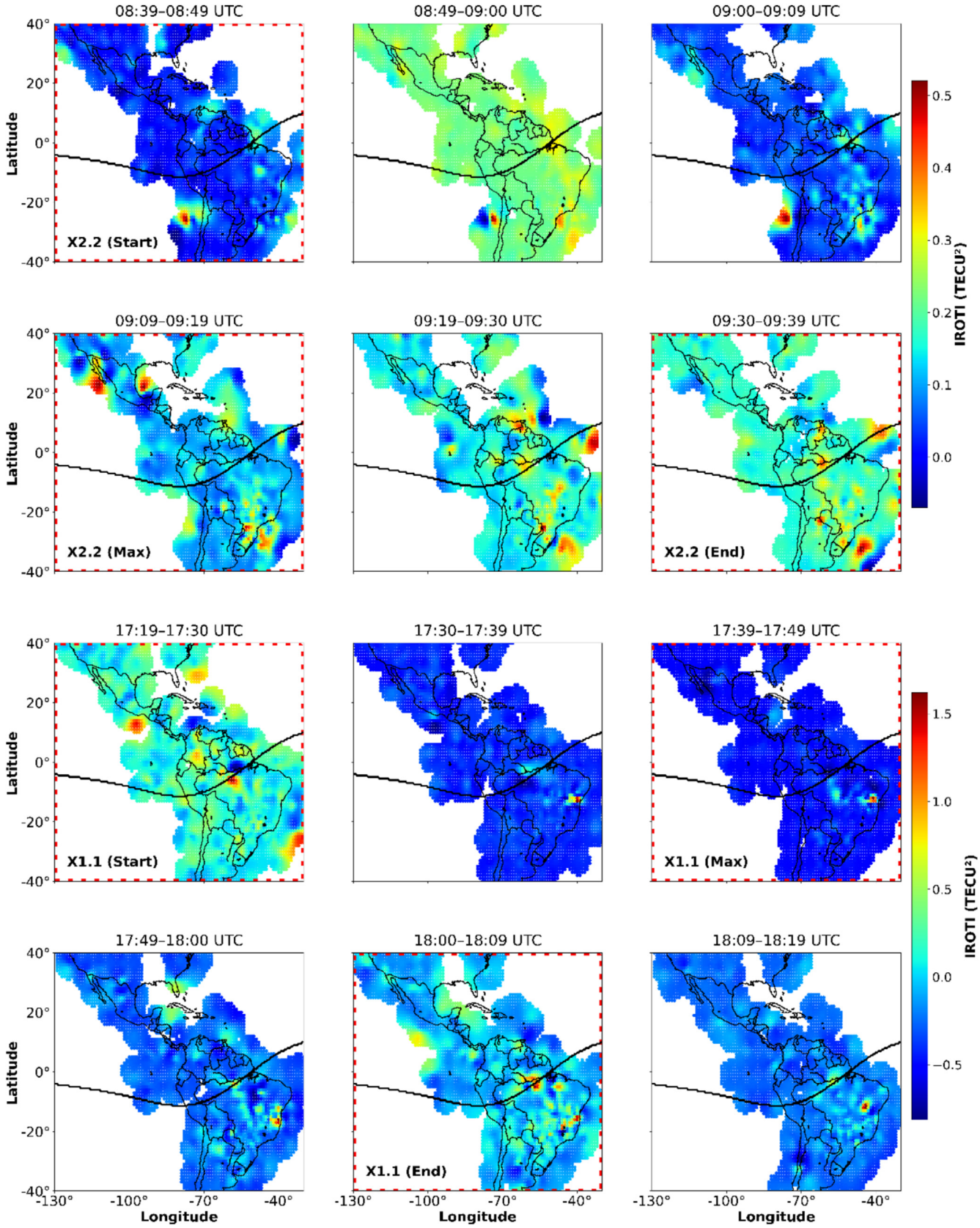

Fig. 12. Represents the 10-min IROTI distribution covering the X2.2 flare that peaked at 09:13 UT (06:13 LT over Brazil) and the X1.1 flare that peaked at 17:44 UT (14:44 LT over Brazil).

LT; Fig. 4a–i), likely because the ionosphere's response to flare radiation varies with local time.

The later X1.1-class flare (S20W32), spanning 17:23–18:01 UT, triggered a distinct NmF2 enhancement that persisted until ~18:15 UT (Fig. 4j–r). The ionospheric reaction exhibited spatial propagation:

- Initial Detection (17:23–17:30 UT / 12:23–12:30 LT): A rapid NmF2 increase was observed over Panama, coinciding with the flare's onset.
- Southeastward Expansion (13:40–13:50 LT): The enhancement extended toward Venezuela and northern Brazil, marked by black-red dots in Fig. 4n.

This delayed response (~1 h post-peak) aligns with the travel time of EUV-induced ionization waves and the local equilibrium timescale in the F2 region (e.g., Qian et al., 2011; Saharan et al., 2023). Similar patterns were observed during other SF events through the studied period (S1–S6), reinforcing the role of flare location, local time, and geomagnetic conditions in modulating ionospheric effects.

3.3. Hemispheric asymmetry and altitude-dependent effects revealed by ionosonde data

The ionosonde stations AU930 (30.4°N, 97.7°W; dip latitude 41.23°N) and CAJ2M (22.7°S, 45°W; dip latitude 17.34°S) are geographically located in low-latitude regions. In geomagnetic coordinates, AU930′s higher dip latitude positions it in the mid-latitude region, while CAJ2M's lower dip latitude places it firmly in the equatorial low-latitude region. This geomagnetic distinction likely influences the observed differences in EDPs. Regarding temporal variations, the stations have a 3.5-h longitudinal time difference (52.7° at 15°/h). However, when AU930 observes Daylight Saving Time (DST; shifting from UTC-6 to UTC-5), the effective offset reduces to 2.5 h relative to CAJ2M (which remains at UTC-3 year-round). As a result, Ne variations typically appear earlier at AU930 in UTC, with the exact timing difference depending on seasonal DST observance.

To assess the impact of geographic and geomagnetic positioning on Ne behavior under quiet conditions, we analyzed ionospheric response on April 3, 2024 (DOY 094), a geomagnetically quiet day (Kp $<$ 3, no SFs or storms). As shown in Fig. 5, CAJ2M exhibited 25 % higher Ne values than AU930, confirming that low-latitude regions generally have higher electron content than mid-latitudes. No significant diurnal variations in Ne were observed when using UTC.

For reference, Figs. 6 and 7 display the full electron density profiles from SAOExplorer, but only the measured bottom-side portion (≤hmF2) was included in our statistical evaluation. The top-side portion (>hmF2) is shown for context only.

Unlike previous studies, our analysis of COSMIC-2 data (Figs. 3 and 4) reveals alternating anomalies between both hemispheres. However, CAJ2M consistently recorded higher Ne values than AU930, except during the peak storm day and the following day. These low-latitude effects in the American sector align with observations of auroral extensions and ionospheric disturbances in Mexico during the May 2024 storm, as reported by Gonzalez-Esparza et al. (2024), though our data emphasize stronger Ne reductions at southern stations such as CAJ2M (69.46 % on DOY 132).

Before the G5 Gannon storm (DOY 130), two disk flares (X2.2, X1.1) were followed by an X3.98 flare on DOY 131, leading to an 84 % increase in Ne at AU930. These flares generated SEPs, X-rays, EUV, and CMEs, culminating in the most intense geomagnetic storm in two decades (Fig. 6b). On DOY 132, the storm's peak, an X5.89 limb flare occurred in the early hours, followed by an X1.5 flare at midday, resulting in a 36 % Ne increase compared to DOY 131 (Fig. 6c). The subsequent four days support the hypothesis that Earth's geomagnetic field requires several days to recover from severe storms (Collado-Villaverde et al., 2024). DOY 133 showed the highest disturbance, with a 44.6 % Ne increase, which gradually declined by approximately 38 %, 45.32 %, and 50.52 % over the next three days (Fig. 6e–g).

The CAJ2M station exhibited behavior as AU930, with significant disturbances on all days except DOYs 132 and 133. However, Ne values at CAJ2M were 28.66 % and 5.88 % higher than at AU930 on the two days preceding the storm. Over the following four days, Ne enhancements relative to DOY 132 were observed, though they gradually decreased compared to DOY 131 by 15 %, 15.36 %, 29.41 %, and 23.86 %, respectively (Fig. 7). On DOY 130, which featured two disk flares (X2.2 and X1.1), Ne at CAJ2M exceeded AU930 by 28.66 %, a greater increase than the 25 % observed under quiet conditions, indicating stronger low-latitude effects from X-class flares compared to mid-latitudes. During DOYs 132 and 133 (the Gannon storm peak and the following day), CAJ2M experienced significant Ne reductions, decreasing by 69.46 % and 37.8 % relative to AU930. In the subsequent three days, Ne at CAJ2M exceeded AU930 by 44.69 %, 36.70 %, and 62.93 % on DOYs 134, 135, and 136, respectively. Notably, no disk flares occurred on DOYs 134 and 135, while an X3.48 flare was observed on DOY 136.

Furthermore, the preceding X-class flares, particularly the X5.89 event on DOY 132, also enhanced D-region ionization, leading to HF radio absorption and ionosonde blackouts lasting 45–90 min over low-to-mid latitudes, as observed globally and consistent with NOAA's R3 blackout alerts (NOAA SWPC, 2024). Our ionosonde records at AU930 and CAJ2M confirmed partial fade-outs in bottom-side echoes during the DOY 130 disk flares (X2.2 and X1.1), aligning with published reports of ~70-min

absorption durations and average minimum frequency increases to 7 (2–12) MHz in similar events (Tulasi Ram et al., 2024). These D-region effects complement our F-region Ne enhancements, underscoring the multi-layer ionospheric response to flares.

The initial impact of the G5 Gannon storm was predominantly directed northward, as confirmed by COSMIC-2 data (Fig. 4d), with Ne in the north exceeding the south by over 50 % on DOY 132. The cascading effects over the following four days were more pronounced at low latitudes, as observed at CAJ2M. This alternating north–south effect is illustrated in Fig. 4.

Our findings indicate that the G5 Gannon storm had a greater impact above 400 km in the northern regions compared to SFs, as shown in Fig. 6a–d. Ionosonde data validated COSMIC-2 observations, revealing more significant storm effects below 300 km at CAJ2M than at AU930. This aligns with Qian et al. (2019), who highlighted altitude- and flare-type-dependent ionospheric responses to geomagnetic storms and SFs. Overall, the study emphasizes the complex, region-specific effects of SFs on ionospheric conditions, with notable differences between low and mid-latitudes in the Northern and Southern regions, enhancing understanding of space weather impacts and ionospheric disruptions.

The following section analyzes ionospheric disturbances induced by the G5 Gannon storm and associated SFs through TEC, ROTI, and IROTI parameters derived from GNSS data across selected geographic stations. The study includes three Northern Hemisphere stations—QUIN (39.975°N, 120.944°W; dip latitude 38.12°N), INEG (21.856°N, 102.284°W; dip latitude 22.91°N), and BOAV (2.854°N, 60.701°W; dip latitude 8.45°N)—and three Southern Hemisphere stations—GLPS (0.743°S, 90.304°W; dip latitude 4.19°S), CHPI (22.687°S, 44.985°W; dip latitude 17.92°S), and MTV1 (34.914°S, 56.176°W; dip latitude 26.96°S)—spanning geographic latitudes from 40°N to 40°S. The analysis covers the storm's main phase and recovery period (DOY 130–136).

3.4. Storm-induced TEC deviations from quiet-time baselines

To quantify ionospheric disturbances during the May 2024 G5-class Gannon storm, we calculated TEC deviations (ΔTEC) by subtracting the average TEC of two quiet days before (DOYs 115 and 116) and two days after the storm (DOYs 142 and 143) from TEC values on disturbed days (DOYs 130–136). Quiet days were selected based on low geomagnetic activity (Kp < 3, Dst < 25). Fig. 8 shows ΔTEC across six IGS stations in the American sector. Mid-latitude stations exhibited distinct responses: QUIN (northern) showed minimal flare effects except for an X8.79 flare (Muniafu et al., 2024), with storm-induced ΔTEC ranging from −3.3 to +5.8 TECU (Foster et al., 2024). MTV1 (southern) displayed stronger flare impacts (~1 TECU) and extreme storm effects (−5.7 to +7.8 TECU), highlighting hemispheric asymmetry (Aa et al., 2024b). Prolonged disturbances occurred due to sustained solar wind speeds >800 km/s (W. Sun et al., 2024).

Equatorial stations (GLPS, BOAV) had smaller variations (±1.5 TECU), reflecting PPEF and dynamo effects (Gonzalez-Esparza et al., 2024; Muniafu et al., 2024). Gonzalez-Esparza et al. (2024) similarly noted low-latitude space weather effects in Mexico, including TEC fluctuations, which support our findings of minimal but persistent disturbances at stations like GLPS during the storm recovery. Low-latitude stations (CHPI, INEG) showed dramatic fluctuations (CHPI: −8 to +9 TECU; INEG: −1.5 to +3.6 TECU), driven by PPEFs and EEJ (Zhang et al., 2025). Flares caused ~1.25 TECU variations at low latitudes, enhanced by 900 km/s solar winds (Rout et al., 2025).

The storm's global and regional impact featured:

- Mid-latitude: Strong storm effects with asymmetric flare responses.
- Equatorial: Moderate changes from electrodynamic processes.
- Low-latitude: Extreme variations from electric fields and TIDs.
- Recovery phase: Extended disturbances from persistent solar wind.

These observations highlight latitude-dependent ionospheric responses to extreme space weather (Aa et al., 2024b).

3.5. Latitudinal dependence of storm and flare impacts on TEC indices

For further clarification, other ionospheric indices are introduced. Fig. 9a–b illustrates the ionospheric response in northern and southern stations, respectively. During the storm's main phase, high-energy particle injection and intensified electric fields led to sharp TEC increases, driven by mechanisms such as the fountain effect and storm-enhanced densities. However, at the same time, it can be noticed that there was a strong ionization depletion at equatorial, low-latitude, and mid-latitude stations in different patterns, as shown in Fig. 9. These significant depletions are due to the merging of the Southern Crest of the EIA with the auroral oval during the May 2024 storm, as confirmed by Karan et al. (2024) and Themens et al. (2024). The merging process coincides with Basu et al.'s (2001) model of storm-time depletion, where poleward-expanding auroral convection drags plasma across latitudes. This simultaneously:

(a) Stretches plasma flux tubes, increasing recombination losses at low latitudes.
(b) Creates density gradients that drive turbulent mixing – explaining the rapid depletions observed at INEG (ROTI > 1.8 TECU/min) and CHPI. These findings highlight the importance of considering both

enhancements and depletions in ionization when analyzing the ionospheric response to geomagnetic storms.

As geomagnetic activity subsided, TEC declined due to enhanced recombination (Verkhoglyadova et al., 2014) and thermospheric cooling (Jakowski et al., 2017, 2024), stabilizing to near-neutral or slightly negative levels by DOYs 133–136. ROTI and IROTI values increased across all stations, indicating widespread ionospheric irregularities. Increases in ROTI during geomagnetic storms are well-documented and reflect enhanced irregularities due to auroral activity, particle precipitation, and ionospheric conductivity enhancements (Cherniak et al., 2022). Mid- and low-latitude stations exhibited significant DTEC increases, while equatorial stations, such as BOAV and GLPS, showed smaller variations, reflecting stronger magnetosphere-ionosphere coupling at higher latitudes. The stronger coupling at higher latitudes results in more pronounced ionospheric effects during geomagnetic storms.

The penetration of electric fields is more significant at mid and high latitudes, whereas the disturbance dynamo primarily affects mid and low latitudes, as it is driven by strong equatorward winds at high latitudes induced by heating at polar and high latitudes during storm/substorm conditions (Astafyeva et al., 2018; Fuller-Rowell et al., 2002).

As geomagnetic activity subsided, TEC declined due to enhanced recombination and thermospheric cooling, stabilizing to near-neutral or slightly negative levels by DOYs 133–136. ROTI and IROTI values increased across all stations, indicating widespread ionospheric irregularities. Mid- and low-latitude stations exhibited significant DTEC increases, while equatorial stations, such as BOAV and GLPS, showed smaller variations, reflecting stronger magnetosphere-ionosphere coupling at higher latitudes.

ROTI clearly separated storm effects from solar flare disturbances in equatorial and low-latitude regions, while IROTI was more sensitive to all latitudes. These findings match earlier studies (e.g., Sun et al., 2021), linking equatorial and low-latitude effects to the equatorial electrojet, PPEFs, and EPB. The Southern Hemisphere's geomagnetic weakness, particularly in regions influenced by the South Atlantic Anomaly (SAA), makes these effects stronger (Aa et al., 2024a; Li et al., 2018).

Higher ROTI and IROTI values in southern stations indicate large-scale TIDs and EPBs, caused by storm-related ionospheric irregularities. For instance, at INEG on DOY 132, ROTI peaked at 1.8 TECU/min and IROTI at 119 $TECU^2$. By DOY 133, these dropped to 1.6 TECU/min and 10 $TECU^2$, showing less disturbance. At BOAV on DOY 130, ROTI peaked at 0.85 TECU/min with IROTI at 3.5 $TECU^2$, then gradually increased before declining during the recovery phase.

These results highlight how ROTI and IROTI work together to measure ionospheric disturbances. ROTI works well for quiet periods and solar flare disturbances, while IROTI is better at detecting changes during the storm's main and initial phases. During recovery, ROTI is more reliable for tracking fluctuations. To fully understand ionospheric behavior during extreme space weather, integrating DTEC, ROTI, and IROTI is essential.

3.6. Distinctive TEC response at equatorial latitudes

To assess the relative impacts of multiple SFs and the most intense geomagnetic storm in over two decades, we analyzed ionospheric disturbances at the equatorial GLPS station (0.74°S, dip latitude ~4.19°S) using DTEC, ROTI, and IROTI (Fig. 10, columns 1–3) from DOY 130 to 136. Key events, including major SFs and the Gannon geomagnetic storm, are marked with black dashed lines for reference.

On DOY 130, localized nighttime irregularities emerged, with ROTI peaking at 0.25 TECU/min and IROTI at 1.5 $TECU^2$, likely associated with EPBs following sunset. Two significant flares (X2.2 and X1.1) occurred that day but induced relatively mild responses—maximum IROTI of 0.75 $TECU^2$—suggesting that EPB dynamics had a stronger influence on ionospheric variability than the flare-driven EUV enhancements. Despite the occurrence of an intense X3.98 disk-centered flare on the morning of DOY 131, pre-storm conditions remained stable. However, a sharp onset of geomagnetic activity at ~17:00 UT triggered immediate ionospheric responses, where the DTEC fluctuated between +4 and −2 TECU, ROTI rose to 0.45 TECU/min, and IROTI spiked to 12 $TECU^2$.

These rapid changes align temporally with the arrival of a CME and the initial shock phase of the G5 storm, indicating the storm's primary role in generating large-scale TIDs and irregularities. On DOY 132, two powerful limb flares (X5.89 and X5.1) occurred, but their effects on DTEC, ROTI, and IROTI were minimal, reinforcing previous findings that limb flares produce weaker ionospheric responses compared to disk-centered flares. Nonetheless, storm-driven effects persisted, sustaining elevated IROTI and moderate TEC variability. The transient X5.89 limb flare (1:10–1:39 UT) exerted minimal ROTI/IROTI impact by its short duration (<30 min) and oblique direction (Tsurutani et al., 2009), while storm effects dominated with persistent PPEF/DDEF. The subsequent 9–10 UT ROTI burst showed correlation with Bz changes, confirming the generation of storm-induced EPB (Astafyeva et al., 2018), unlike the weak, local ionospheric flare response.

The ionospheric response intensified on DOYs 133 and 134, likely influenced by additional CME arrivals during the night. Compared to pre-storm levels, the ROTI tripled, the IROTI increased by 3.5×, and TEC depletion doubled. Although no major flares were recorded on DOY 134, disturbances exceeded those from the prior day. This pattern echoes Zhang et al. (2011), who showed that disk-centered flares produce more significant ionospheric impacts than limb flares of the same X-ray classification.

DOY 135 featured three moderate-to-intense flares (X1.72, X1.2, and X8.79). However, the ionospheric response remained subdued, where the IROTI increased only slightly—from 0.2 to 0.55 $TECU^2$ post-X1.2 and to 0.7 $TECU^2$ after the X8.79 flare. Despite its intensity, the X8.79 flare induced a far weaker response than the geomagnetic storm, further confirming the dominant role of storm-time electric fields and particle precipitation.

For further clarification, the sharp increases in ROTI/IROTI observed at the GLPS station at 9–10 UT (DOY 132) and 3–6 UT (DOY 133–134) can be attributed to storm-modified equatorial dynamics. The delayed peak at 9–10 UT followed fluctuations in the IMF Bz, which varied from −46.5 nT to +13.7 nT and then back to −36.3 nT. These fluctuations enhanced the PPEFs, leading to the formation of atypical dawn-sector plasma bubbles (EPBs) (Astafyeva et al., 2018; Karan et al., 2024; Kelley et al., 2003).

The subsequent enhancements between 3 and 6 UT coincided with sustained solar wind speeds exceeding 800 km/s, which drove DDEFs. These effects generated post-midnight irregularities, despite the Dst values indicating a recovery phase (Blanc & Richmond, 1980). The initial suppression of ROTI (≤0.5 TECU/min) after the storm reflects the dominance of large-scale total electron content (TEC) changes before smaller-scale (~1–10 km) irregularities emerged through nonlinear EPB growth (Zakharenkova et al., 2018).

While some studies report immediate post-storm scintillation (e.g., Basu et al., 2001), our observations correspond with modeled delays of 6–8 h for EPB growth during complex variations in Bz (Carter et al., 2014). On DOY 136, although solar activity was minimal, lingering storm effects were evident in nighttime ROTI and IROTI enhancements, pointing to the persistence of EPBs and residual TIDs beyond the main recovery phase.

The GLPS analysis highlights the complex interplay between solar flares and geomagnetic storms in modulating equatorial ionospheric conditions. Disk-centered flares produced stronger short-term effects than limb flares, but the G5 storm had the most significant and sustained impact—especially evident in elevated IROTI values. These results demonstrate that while solar flares can contribute to ionospheric variability, major geomagnetic storms act as dominant drivers, with post-storm irregularities often outlasting flare-related perturbations. Comprehensive monitoring using DTEC, ROTI, and IROTI is essential for disentangling the overlapping effects of different space weather drivers.

3.7. Detection of irregularities using the IROTI index

Fig. 11 presents the spatial and temporal evolution of IROTI across the American sector during DOYs 130 to 136, segmented into 4-h intervals. This analysis highlights the impact of the G5 Gannon storm and concurrent SFs on the ionosphere. Each panel corresponds to a specific DOY, with annotations detailing the intensity of major solar events. The black dotted box emphasizes the critical time interval (08:00–12:00 UT) on DOYs 132 and 133, capturing the storm's peak and subsequent recovery.

High IROTI values, shown in red, indicate significant small-scale ionospheric irregularities that can disrupt satellite signals and navigation systems. This figure improves on earlier studies (e.g., Qian et al., 2012; Zhang et al., 2011) by capturing both spatial and longitudinal effects. The geomagnetic disturbance started on DOY 131 at 17:00 UT and peaked at 22:54 UT. During the main phase, IROTI values sharply increased, peaking at 131.83 $TECU^2$ in the final panel for DOY 131. This peak matches the growth of EPBs and TIDs, which started in the Southern Hemisphere and spread to both hemispheres. The propagation patterns suggest strong coupling between geomagnetic activity and ionospheric disturbances, consistent with the ionospheric puzzles and duskside electrodynamic forcing observed by Astafyeva et al. (2024) during the same storm, which may explain the hemispheric spread of EPBs in our IROTI maps (Fig. 11). Ren et al. (2024) classify disturbances as EPBs when IROTI values exceed 7.28 TECU2 and as TIDs when values fall below 4.91 TECU2. Based on these thresholds, DOY 131 experienced widespread EPB activity, particularly during the storm's main phase, while subsequent days (e.g., DOY 132) exhibited a gradual transition to TID-dominated irregularities. Notably, during the recovery phase, IROTI values dropped below 20 TECU2, as shown in the final panels of DOY 132.

The analysis shows complex interactions between SFs and geomagnetic storms. For instance, on DOY 132, an X1.5 limb flare peaked at 11:44 UT, but IROTI values remained moderate, indicating less impact than the earlier storm. Conversely, disk flares on DOY 130 had a stronger effect, with much higher IROTI values in the fourth and fifth panels.

DOY 133 marked the transition to the recovery phase, characterized by lower frequencies of ionospheric disturbances and moderate IROTI peaks (~47 $TECU^2$). Although an X1.02 limb flare occurred near sunset, its impact was limited, likely due to reduced ionospheric conductivity at that time. However, clusters of elevated IROTI values persisted, particularly in the late evening, emphasizing the lingering effects of the Gannon storm in enhancing EPB activity.

Nighttime enhancements, driven by storm-induced plasma instabilities, were prominent across DOYs 134 to 136, as evidenced by elevated IROTI values (~65 TECU2) despite the absence of significant flares. This observation underscores the dominant role of geomagnetic storms, particularly in regions affected by the SAA. The panels for 08:00–12:00 UT across all DOYs reveal a clear distinction between the ionospheric effects of intense SFs and the Gannon storm. DOYs 134 to 136 mirrored the spatial patterns observed during DOYs 130 and 131, while DOYs 132 and 133 exhibited heightened TEC densities, particularly during the storm's peak and immediate aftermath.

This analysis demonstrates the utility of IROTI in extracting the complex interplay between SFs and geomagnetic storms. While SFs exert localized impacts, the Gannon storm induced widespread, persistent ionospheric irregularities, particularly in the Southern Hemisphere. The integration of IROTI with other parameters, such as ROTI and DTEC, offers a comprehensive framework for understanding ionospheric dynamics during extreme space weather events. Additionally, for a deep understanding of SFs' rapid impact on the low- to mid-latitude ionosphere, a 10-min time window evaluation has been discussed through DOY 130, which has two disk flares as an example.

SFs are defined as rapid and strong bursts of electromagnetic radiation from the Sun, primarily at X-ray and EUV wavelengths. These bursts can have a major impact on the Earth's ionosphere within minutes, particularly in low-latitude regions where ionospheric electrodynamics are highly sensitive to solar inputs (Tsurutani et al., 2005). According to prior research, the IROTI Index is an effective proxy for detecting rapid changes in electron concentration and, as a result, short-term ionospheric disturbances caused by SFs.

For example, Fig. 12 shows the IROTI response in the American low-latitude region to two major disk-center SFs on DOY 130 (May 9, 2024): the X2.2 flare peaking at 09:13 UT and the X1.1 flare peaking at 17:44 UT. While both flares triggered noticeable responses, a striking observation is that the IROTI values during the X2.2 event remained relatively low (mostly < 0.35 TECU^2). In contrast, during the X1.1 flare, values exceeded 1.3 TECU^2, as clearly shown by the respective color bars.

Further research is necessary to understand this puzzling finding, which indicates that a weaker X1.1 flare produced a stronger ionospheric irregularity signal than the stronger X2.2 flare.

a) Temporal Context and Preconditioning

A key factor may lie in the preconditioning of the ionosphere. The X2.2 event occurred early in the day (around 06:13 LT in Brazil), when the equatorial ionosphere is still forming post-sunrise. During this time, the ionospheric plasma density is still increasing, and the equatorial electrodynamics—particularly the pre-reversal enhancement and equatorial plasma fountain—have not fully developed (Kelley and Heelis, 2009). Consequently, the background conditions may have been less favorable for plasma instability growth and irregularity formation, leading to lower IROTI values despite a strong flare.

The X1.1 flare, on the other hand, occurred around 14:44 LT, closer to the local pre-sunset time when the ionospheric plasma is highly organized and more vulnerable to Rayleigh-Taylor instabilities, which cause equatorial spread-F and irregularities (Woodman and Hoz, 1976). Thus, even a somewhat strong flare, such as X1.1, might result in much higher IROTI readings under these conditions.

b) Flare Position and Geoeffectiveness

Although both flares were observed near the disk center—typically implying strong geoeffectiveness—the relative spectral composition (X-ray vs. EUV dominance), duration, and background geomagnetic activity can also modulate the response. According to Yadav et al. (2016), if an X-flare occurs during a low TEC background or under pre-storm quiet conditions (as was the case before the Gannon storm on DOY 131), its perturbation may not be strongly amplified. This could further explain the muted IROTI during X2.2.

Our results are consistent with studies that highlight the local time dependence of flare impacts: Bagiya et al. (2011) reported stronger ionospheric responses to moderate flares during the afternoon over Indian equatorial regions, while Afraimovich et al. (2001) demonstrated minimal ionospheric responses to strong flares in the early morning. Furthermore, López-Montes et al. (2012) and Ryakhovsky et al. (2024) showed that TEC sensitivity is influenced by electrodynamic background circumstances in addition to flare intensity.

Because of this, the ionospheric condition at the time of the X2.2 flare was not primed for irregularity creation, which led to lower IROTI values even though the flare was more intense in solar classification. The X1.1 flare, on the other hand, was weaker but happened during a high-instability window, which allowed for more GNSS signal variations and more plasma structuring.

The significance of local time, ionospheric preconditioning, and background electrodynamics in regulating the ionospheric reaction to SFs is shown by this analysis. The fewer X1.1 flares, the stronger the IROTI signals, indicating that contextual geophysical variables are a crucial factor in predicting ionospheric impact, and flare classification alone is insufficient. Capturing these fleeting but important responses requires high-temporal-resolution data, such as IROTI in 10-min periods.

4. Conclusion

The May 2024 G5-class Gannon storm and associated X-class solar flares provided a unique opportunity to investigate ionospheric responses in low-to-mid latitude regions (40°S to 40°N) across the American sector. Utilizing FORMOSAT-7/COSMIC-2 radio occultation profiles, ground-based ionosonde measurements, and GNSS-derived TEC data, this study revealed significant ionospheric disturbances driven by complex interactions between solar flares (SFs) and geomagnetic activity. Electron density (Ne) exhibited pronounced enhancements, with increases of 137.7 % above 300 km in the northern hemisphere (0°–40°N) and 129.2 % around 200 km in the southern hemisphere (0°–40°S) during the storm's peak on May 11 (DOY 132), compared to quiet-time conditions on May 8 (DOY 129). Disk flares had a stronger impact on low-latitude regions, elevating Ne by 28.66 %, while

geomagnetic storms predominantly affected mid-latitudes, with Ne increases of 44.6 % during the storm's peak (Dst = –518 nT). Hemispheric asymmetries were evident, likely driven by the southward displacement of the geomagnetic equator, prompt penetration electric fields (PPEFs), and thermospheric winds.

The IROTI index, defined as the product of integral DTEC (IDTEC) and Rate of TEC Index (ROTI), proved more effective than DTEC or ROTI alone in distinguishing the impacts of SFs and geomagnetic storms, particularly during the main phase of the May 2024 G5-class Gannon storm. IROTI highlighted widespread EPBs and TIDs, with peak values of 131.83 TECU2 on DOY 131, reflecting significant small-scale irregularities. While ROTI was more reliable during storm recovery, IROTI captured broader disturbance patterns, especially in equatorial and low-latitude regions. Disk flares induced rapid, localized Ne and TEC enhancements, whereas the Gannon storm drove persistent, hemisphere-asymmetric perturbations, influenced by the SAA. A multi-index approach combining IROTI, DTEC, and ROTI provides a comprehensive framework for understanding ionospheric dynamics during extreme space weather events. While TEC variations in specific bands (e.g., 10–20 min for TIDs) may offer targeted insights, IROTI's integrated metric enhances detection of complex irregularities. Ongoing validation of IROTI's advantages will further refine its application in improving GNSS positioning accuracy, particularly in densely populated low-to-mid latitude regions.

Declaration of competing interest

The authors declare that they have no known competing financial interests or personal relationships that could have appeared to influence the work reported in this paper.

Acknowledgments

This research was funded by the National Natural Science Foundation of China (no. 42230104), the National Science Fund for Distinguished Young Scholars of China (no. 42425003), and the National Natural Science Foundation of China (no. 42388102). The numerical calculations have been done on the supercomputing system in the Supercomputing Center of Wuhan University.

Data Availability

The data used in this study are publicly available. COSMIC-2 data are from the COSMIC Data Analysis and Archive Center (CDAAC) at https://data.cosmic.ucar.edu/gnss-ro/cosmic2/provisional/spaceWeather/level2/. The ionosonde data are from the Digital Ionogram Database (DIDBase) at ftp.ngdc.noaa.gov/ionosonde/. Total Electron Content data were derived from RINEX observations obtained from the IGS network (https://cddis.nasa.gov/archive/gnss/data/) and the Brazilian Continuous Monitoring Network (RBMC) (ftp://geoftp.ibge.gov.br/). Space weather indices are from https://wdc.kugi.kyoto-u.ac.jp/aeasy/index.html and https://omniweb.gsfc.nasa.gov/form/dx1.html.

Appendix A. Supplementary material

Supplementary data to this article can be found online at https://doi.org/10.1016/j.asr.2025.10.023.

References

Aa, E., Coster, A.J., Zhang, S.R., Vierinen, J., Erickson, P.J., Goncharenko, L.P., Rideout, W., 2024a. 2-D total electron content and 3-D ionospheric electron density variations during the 14 October 2023 annular solar eclipse. J. Geophys. Res. Space Phys. 129 (3). https://doi.org/10.1029/2024JA032447.

Aa, E., Chen, Y., Luo, B., 2024b. Dynamic expansion and merging of the equatorial ionization anomaly during the 10–11 May 2024 super geomagnetic storm. Remote Sens. (Basel) 16 (22), 1–16. https://doi.org/10.3390/rs16224290.

Abdelaziz, A., Ren, X., Hosny, M., Mei, D., Le, X., Liu, H., Zhang, X., 2025. Global ionospheric F-layer electron density prediction based on multiple radio occultation data using attention-based deep learning model. IEEE Trans. Geosci. Remote Sens. 63, 1–16. https://doi.org/10.1109/TGRS.2025.3546248.

Afraimovich, E.L., Altynsev, A.T., Grechnev, V.V., Leonovich, L.A., 2001. Ionospheric effects of the solar flares as deduced from global GPS network data. Adv. Space Res. 27 (6–7), 1333–1338. https://doi.org/10.1016/S0273-1177(01)00172-7.

Alfonsi, L., Cesaroni, C., Spogli, L., Regi, M., Paul, A., Ray, S., et al., 2021. Ionospheric disturbances over the Indian sector during 8 September 2017 geomagnetic storm: plasma structuring and propagation. Space Weather 19 (3), 1–16. https://doi.org/10.1029/2020SW002607.

Arslan Tariq, M., Liu, L., Shah, M., Yang, Y., Sun, W., Ali Shah, M., et al., 2024. Longitudinal variations of ionospheric responses to the February and April 2023 geomagnetic storms over American and Asian sectors. Adv. Space Res. 73 (6), 3033–3049. https://doi.org/10.1016/j.asr.2023.12.039.

Astafyeva, E., Zakharenkova, I., Hozumi, K., Alken, P., Coïsson, P., Hairston, M.R., Coley, W.R., 2018. Study of the equatorial and low-latitude electrodynamic and ionospheric disturbances during the 22–23 June 2015 geomagnetic storm using ground-based and spaceborne techniques. J. Geophys. Res. Space Phys. 123 (3), 2424–2440. https://doi.org/10.1002/2017JA024981.

Astafyeva, E., Maletckii, B., Förster, M., Ouar, I.D., Huba, J.D., Hairston, M.R., Coley, W.R., 2025. Electrodynamic and ionospheric puzzles of the 10–11 May 2024 geomagnetic superstorm. J. Geophys. Res. Space Phys. 130 (5). https://doi.org/10.1029/2024JA033284.

Bagiya, M.S., Iyer, K.N., Joshi, H.P., Thampi, S.V., Tsugawa, T., Ravindran, S., et al., 2011. Low-latitude ionospheric-thermospheric response to storm time electrodynamical coupling between high and low latitudes. J. Geophys. Res. Space Phys. 116 (1), 1–17. https://doi.org/10.1029/2010JA015845.

Basu, S., Basu, S., Groves, K.M., Yeh, H.C., Su, S.Y., Rich, F.J., et al., 2001. Response of the equatorial ionosphere in the South Atlantic region to the great magnetic storm of July 15, 2000. Geophys. Res. Lett. 28 (18), 3577–3580. https://doi.org/10.1029/2001GL013259.

Besliu-Ionescu, D., Maris Muntean, G., Dobrica, V., 2022. Complex catalogue of high speed streams associated with geomagnetic storms during solar cycle 24. Sol. Phys. 297 (5). https://doi.org/10.1007/s11207-022-01998-3.

Blanc, M., Richmond, A.D., 1980. The ionospheric disturbance dynamo. J. Geophys. Res. Space Phys. 85 (9), 1669–1686. https://doi.org/10.1029/JA085iA04p01669.

Blewitt, G., 2008. Fixed point theorems of GPS carrier phase ambiguity resolution and their application to massive network processing: Ambizap. J. Geophys. Res. Solid Earth 113 (12), 1–12. https://doi.org/10.1029/2008JB005736.

Carter, B.A., Retterer, J.M., Yizengaw, E., Groves, K., Caton, R., McNamara, L., et al., 2014. Geomagnetic control of equatorial plasma bubble activity modeled by the TIEGCM with Kp. Geophys. Res. Lett. 41 (15), 5331–5339. https://doi.org/10.1002/2014GL060953.

Cherniak, I., Zakharenkova, I., Krankowski, A., 2022. IGS ROTI maps: current status and its extension towards equatorial region and southern hemisphere. Sensors 22 (10), 1–17. https://doi.org/10.3390/s22103748.

Ciraolo, L., Azpilicueta, F., Brunini, C., Meza, A., Radicella, S.M., 2007. Calibration errors on experimental slant total electron content (TEC) determined with GPS. J. Geod. 81 (2), 111–120. https://doi.org/10.1007/s00190-006-0093-1.

Collado-Villaverde, A., Muñoz, P., Cid, C., 2024. Classifying and bounding geomagnetic storms based on the SYM-H and ASY-H indices. Nat. Hazards 120 (2), 1141–1162. https://doi.org/10.1007/s11069-023-06241-1.

Dal Poz, W.R., Silva, A.C., Dos Santos, A.D.P., Medeiros, N.D.G., Ferreira, Í.O., de Oliveira, J.C., 2025. Impacts of the great May 2024 geomagnetic storm on precise point positioning. Revista Brasileira de Geografia Fisica 18 (3), 1697–1713. https://doi.org/10.26848/rbgf.v18.3.p1697-1713.

Danilchuk, E., Yasyukevich, Y., Vesnin, A., Klyusilov, A., Zhang, B., 2025. Impact of the May 2024 extreme geomagnetic storm on the ionosphere and GNSS positioning. Remote Sens. (Basel) 17 (9), 1492. https://doi.org/10.3390/rs17091492.

Foster, J.C., Erickson, P.J., Nishimura, Y., Zhang, S.R., Bush, D.C., Coster, A.J., et al., 2024. Imaging the May 2024 extreme aurora with ionospheric total electron content. Geophys. Res. Lett. 51 (20). https://doi.org/10.1029/2024GL111981.

Foster, J.C., 1993. Storm time plasma transport at middle and high latitudes. J. Geophys. Res. Space Phys. 98 (A2), 1675–1689. https://doi.org/10.1029/92ja02032.

Fuller-Rowell, T.J., Codrescu, M.V., 1994. Response of the thermosphere and ionosphereto geomagnetic storms. J. Geophys. Res. 99 (A3), 3893–3914. https://doi.org/10.1029/93JA02015.

Fuller-Rowell, T.J., Millward, G.H., Richmond, A.D., Codrescu, M.V., 2002. Storm-time changes in the upper atmosphere at low latitudes. J. Atmos. Sol. Terr. Phys. 64 (12–14), 1383–1391. https://doi.org/10.1016/S1364-6826(02)00101-3.

Gonzalez-Esparza, J.A., Sanchez-Garcia, E., Sergeeva, M., Corona-Romero, P., Gonzalez-Mendez, L.X., Valdes-Galicia, J.F., et al., 2024. The Mother's Day geomagnetic storm on 10 May 2024: aurora observations and low latitude space weather effects in Mexico. Space Weather 22 (11), 1–17. https://doi.org/10.1029/2024SW004111.

Hajra, R., Tsurutani, B.T., Lakhina, G.S., Lu, Q., Du, A., 2024. Interplanetary causes and impacts of the 2024 May superstorm on the geosphere: an overview. Astrophys J 264 https://arxiv.org/abs/2408.14799v1.

Hapgood, M., Liu, H., Lugaz, N., 2022. SpaceX—sailing close to the space weather?. Space Weather 20 (3), 1–2. https://doi.org/10.1029/2022SW003074.

He, J., Yue, X., Le, H., Ren, Z., Ding, F., 2022. High-resolution and accurate low-latitude gridded electron density generation and evaluation. J. Geophys. Res. Space Phys. 127 (4), 1–15. https://doi.org/10.1029/2021JA030192.

Jakowski, N., Mainul Hoque, M., Mielich, J., Hall, C., 2017. Equivalent slab thickness of the ionosphere over Europe as an indicator of long-term temperature changes in the thermosphere. J. Atmos. Sol. Terr. Phys. 163, 91–102. https://doi.org/10.1016/j.jastp.2017.04.008.

Jakowski, N., Hoque, M.M., Mielich, J., 2024. Long-term relationships of ionospheric electron density with solar activity. J. Space Weather Space Clim. 14. https://doi.org/10.1051/swsc/2024023.

Karan, D.K., Martinis, C.R., Daniell, R.E., Eastes, R.W., Wang, W., McClintock, W.E., et al., 2024. GOLD observations of the merging of the southern crest of the equatorial ionization anomaly and aurora during the 10 and 11 May 2024 Mother's Day super geomagnetic storm. Geophys. Res. Lett. 51 (15). https://doi.org/10.1029/2024GL110632.

Kelley, M.C., Heelis, R.A., 2009. In: The Earth's Ionosphere - Plasma Physics and Electrodynamics, second ed. Academic Press, San Diego, California. https://doi.org/10.1016/B978-0-12-088425-4.50001-4.

Kelley, M.C., Makela, J.J., Chau, J.L., Nicolls, M.J., 2003. Penetration of the solar wind electric field into the magnetosphere/ionosphere system. Geophys. Res. Lett. 30 (4), 23–25. https://doi.org/10.1029/2002GL016321.

Li, G., Ning, B., Wang, C., Abdu, M.A., Otsuka, Y., Yamamoto, M., et al., 2018. Storm-enhanced development of postsunset equatorial plasma bubbles around the Meridian 120°E/60°W on 7–8 September 2017. J. Geophys. Res. Space Phys. 123 (9), 7985–7998. https://doi.org/10.1029/2018JA025871.

Li, T., Zheng, D., He, C., Ye, F., Yuan, P., Yao, Y., et al., 2025. Ionospheric response to the 24–27 February 2023 solar flare and geomagnetic storms over the European region using a machine learning–based tomographic technique. Space Weather 23 (1), 1–22. https://doi.org/10.1029/2024SW004146.

Liu, J.Y., Lin, C.H., Chen, Y.I., Lin, Y.C., Fang, T.W., Chen, C.H., et al., 2006. Solar flare signatures of the ionospheric GPS total electron content. J. Geophys. Res. Space Phys. 111 (5), 2–7. https://doi.org/10.1029/2005JA011306.

Liu, J.Y., Chen, C.Y., Sun, Y.Y., Lee, I.T., Chum, J., 2019. Fluctuations on vertical profiles of the ionospheric electron density perturbed by the March 11, 2011 M9.0 Tohoku earthquake and tsunami. GPS Solut. 23 (3), 1–10. https://doi.org/10.1007/s10291-019-0866-7.

López-Montes, R., Pérez-Enríquez, R., Araujo-Pradere, E.A., 2012. The impact of large solar events on the total electron content of the ionosphere at mid latitudes. Adv. Space Res. 49 (7), 1167–1179. https://doi.org/10.1016/j.asr.2012.01.008.

Maletckii, B., Yasyukevich, Y., Vesnin, A., 2020. Wave signatures in total electron content variations: filtering problems. Remote Sens. (Basel) 12 (8), 1–16. https://doi.org/10.3390/RS12081340.

Mawad, R., 2024. The study of angular distance distribution to the solar flares during different solar cycles. AAPPS Bull. 34 (1). https://doi.org/10.1007/s43673-023-00102-6.

Morozova, A.L., Barlyaeva, T.V., Barata, T., 2020. Variations of TEC over Iberian Peninsula in 2015 due to geomagnetic storms and solar flares. Space Weather 18 (11). https://doi.org/10.1029/2020SW002516.

Muniafu, W., Uluma, E., Lomotey, S.O., Nguessan, K., Bankole, F.J., Uga, C.I., et al., 2024. Ionospheric total electron content response to the intense geomagnetic storm of 10th–11th May 2024 over low, mid and high latitude regions. Asian J. Res. Rev. Phys. 8 (4), 19–36. https://doi.org/10.9734/ajr2p/2024/v8i4172.

Nagovitsyn, Y.A., Ivanov, V.G., 2023. Solar cycle pairing and prediction of cycle 25. Sol. Phys. 298 (3), 1–11. https://doi.org/10.1007/s11207-023-02121-w.

Nava, B., Kashcheyev, A., Radicella, S.M., Fleury, R., 2016. J. Geophys. Res.: Space Phys., 3421–3438 https://doi.org/10.1002/2015JA022299. Received.

NOAA SWPC, 2024. Solar Flares (Radio Blackouts). Retrieved from https://www.swpc.noaa.gov/phenomena/solar-flares-radio-blackouts.

Pansong, C., Wongsak, P., Ruttanaburee, S., Pornsopin, P., Kenpankho, P., 2025. Low latitude TEC disturbances during extreme geomagnetic storms: insights into March and May 2024. Adv. Space Res. https://doi.org/10.1016/j.asr.2025.03.071.

Peng, Y.X., Scales, W.A., Hartinger, M.D., Xu, Z., Coyle, S., 2021. Characterization of multi-scale ionospheric irregularities using ground-based and space-based GNSS observations. Satell. Navig. 2 (1). https://doi.org/10.1186/s43020-021-00047-x.

Pi, X., Mannucci, A.J., Lindqwister, U.J., Ho, C.M., 1997. Monitoring of global ionospheric irregularities using the worldwide GPS network. Geophys. Res. Lett. 24 (18), 2283–2286. https://doi.org/10.1029/97GL02273.

Prölss, G.W., 1995. Ionospheric F-region storms. In: Handbook of Atmospheric Electrodynamics, first ed. CRC Press, p. 54. https://doi.org/10.1201/9780203713297.

Qian, L., Burns, A.G., Chamberlin, P.C., Solomon, S.C., 2011. Variability of thermosphere and ionosphere responses to solar flares. J. Geophys. Res. Space Phys. 116 (10), 1–14. https://doi.org/10.1029/2011JA016777.

Qian, L., Burns, A.G., Liu, H., Chamberlin, P.C., 2012. Effect of a solar flare on a traveling atmospheric disturbance. J. Geophys. Res. Space Phys. 117 (10), 1–8. https://doi.org/10.1029/2012JA017806.

Qian, L., Wang, W., Burns, A.G., Chamberlin, P.C., Coster, A., Zhang, S. R., Solomon, S.C., 2019. Solar flare and geomagnetic storm effects on the thermosphere and ionosphere during 6–11 September 2017. J. Geophys. Res. Space Phys. 124 (3), 2298–2311. https://doi.org/10.1029/2018JA026175.

Qian, L., Wang, W., Burns, A.G., Chamberlin, P.C., Solomon, S.C., 2020. Responses of the thermosphere and ionosphere system to concurrent solar flares and geomagnetic storms. J. Geophys. Res. Space Phys. 125 (3), 1–14. https://doi.org/10.1029/2019JA027431.

Schunk, R.W., Nagy, A.F., 2009. Ionospheres Physics, Plasma Physics, and Chemistry, second ed. Cambridge University Press, New York.

Reinisch, B.W., Galkin, I.A., 2011. Global ionospheric radio observatory (GIRO). Earth Planets Space, 377–381. https://doi.org/10.5047/eps.2011.03.001.

Ren, X., Le, X., Mei, D., Liu, H., Zhang, X., 2024. IROTI: a new index to detect and identify traveling ionospheric disturbances and equatorial plasma bubbles. GPS Solut. 28 (1), 1–13. https://doi.org/10.1007/s10291-023-01545-y.

Rout, D., Kumar, A., Singh, R., Patra, S., Karan, D.K., Chakraborty, S., et al., 2025. Evidence of unusually strong equatorial ionization anomaly at three local time sectors during the Mother's Day geomagnetic storm on 10–11 May 2024. Geophys. Res. Lett. 52 (2). https://doi.org/10.1029/2024GL111269.

Ryakhovsky, I.A., Poklad, Y.V., Gavrilov, B.G., Bekker, S.Z., 2024. Estimation of the ionospheric D-region ionization caused by X-class solar flares based on VLF observations. J. Geophys. Res. Space Phys. 129 (6), 1–11. https://doi.org/10.1029/2023JA031532.

Saharan, S., Maurya, A.K., Dube, A., Patil, O.M., Singh, R., Sharma, H., 2023. Low latitude ionospheric TEC response to the solar flares during the peak of solar cycle 24. Adv. Space Res. 72 (9), 3890–3902. https://doi.org/10.1016/j.asr.2023.07.015.

Saito, A., Fukao, S., Miyazaki, S., 1998. High resolution mapping of TEC perturbations with the GSI GPS network over Japan. Geophys. Res. Lett. 25 (16), 3079–3082. https://doi.org/10.1029/98GL52361.

Song, X., Yang, R., Zhan, X., Fu, N., Yang, Z., Yu, X., 2022. Vertical characterization on global ionospheric variations during the magnetic storm in September 2017 with hierarchical subtraction method. Adv. Space Res. 69 (3), 1380–1392. https://doi.org/10.1016/j.asr.2021.11.034.

Sun, L.C., Xu, J.Y., Zhu, Y.J., Yuan, W., Zhao, X.K., 2021. Case study of an Equatorial Plasma Bubble Event investigated by multiple ground-based instruments at low latitudes over China. Earth Planet. Phys. 5 (5), 435–449. https://doi.org/10.26464/epp2021048.

Sun, W., Li, G., Zhang, S.R., Zhao, B., Li, Y., Tariq, M.A., et al., 2024. Complex ionospheric fluctuations over East and Southeast Asia during the May 2024 super geomagnetic storm. J. Geophys. Res. Space Phys. 129 (12), 1–14. https://doi.org/10.1029/2024JA033096.

Themens, D.R., Elvidge, S., McCaffrey, A.M., Jayachandran, P.T., Coster, A., Varney, R.H., et al., 2024. The high latitude ionospheric response to the major May 2024 geomagnetic storm: a synoptic view. Authorea Preprints. https://doi.org/10.1029/2024GL111677.

Tsurutani, B.T., Verkhoglyadova, O.P., Mannucci, A.J., Saito, A., Araki, T., Yumoto, K., et al., 2008. Prompt penetration electric fields (PPEFs) and their ionospheric effects during the great magnetic storm of 30–31 October 2003. J. Geophys. Res. Space Phys. 113 (5), 1–10. https://doi.org/10.1029/2007JA012879.

Tsurutani, B.T., Verkhoglyadova, O.P., Mannucci, A.J., Lakhina, G.S., Li, G., Zank, G.P., 2009. A brief review of "solar flare effects" on the ionosphere. Radio Sci. 44 (4), 1–14. https://doi.org/10.1029/2008RS004029.

Tsurutani, B.T., Judge, D.L., Guarnieri, F.L., Gangopadhyay, P., Jones, A.R., Nuttall, J., et al., 2005. The October 28, 2003 extreme EUV solar flare and resultant extreme ionospheric effects: comparison to other Halloween events and the Bastille Day event. Geophys. Res. Lett. 32 (3), 1–4. https://doi.org/10.1029/2004GL021475.

Tulasi Ram, S., Veenadhari, B., Dimri, A.P., Bulusu, J., Bagiya, M., Gurubaran, S., et al., 2024. Super-intense geomagnetic storm on 10–11 May 2024: possible mechanisms and impacts. Space Weather 22 (12). https://doi.org/10.1029/2024SW004126.

Verkhoglyadova, O.P., Tsurutani, B.T., Mannucci, A.J., Mlynczak, M.G., Hunt, L.A., Paxton, L.J., 2014. Ionospheric TEC, thermospheric cooling and $\sigma[O/N_2]$ compositional changes during the 6–17 March 2012 magnetic storm interval (CAWSES II). J. Atmos. Sol. Terr. Phys. 115–116, 41–51. https://doi.org/10.1016/j.jastp.2013.11.009.

Wang, Y., Yuan, Y., Li, M., Zhang, T., Geng, H., Wang, G., Wen, G., 2023. Effects of strong geomagnetic storms on the ionosphere and degradation of precise point positioning accuracy during the 25th solar cycle rising phase: a case study. Remote Sens. (Basel) 15 (23). https://doi.org/10.3390/rs15235512.

Woodman, R.F., Hoz, C.L., 1976. HF radar observations of irregularities in the daytime equatorial F region. J. Geophys. Res. 81 (31), 5447–5466. https://doi.org/10.1029/JA081i031p05447.

Yadav, S., Sunda, S., Sridharan, R., 2016. The impact of the 17 March 2015 St. Patrick's Day storm on the evolutionary pattern of equatorial ionization anomaly over the Indian longitudes using high-resolution spatiotemporal TEC maps: new insights. Space Weather 14 (10), 786–801. https://doi.org/10.1002/2016SW001408.

Zakharenkova, I.E., Cherniak, I.V., Shagimuratov, I.I., Klimenko, M.V., 2018. Features of high-latitude ionospheric irregularities development as revealed by ground-based GPS observations, satellite-borne GPS observations and satellite in situ measurements over the territory of Russia during the geomagnetic storm on March 17–18, 20. Geomag. Aeron. 58 (1), 70–82. https://doi.org/10.1134/S0016793217050176.

Zhang, D.H., Mo, X.H., Cai, L., Zhang, W., Feng, M., Hao, Y.Q., Xiao, Z., 2011. Impact factor for the ionospheric total electron content response to solar flare irradiation. J. Geophys. Res. Space Phys. 116 (4), 1–8. https://doi.org/10.1029/2010JA016089.

Zhang, R., Liu, L., Yue, X., Zhang, J., Zhang, N., Chen, Y., et al., 2025. The penetration electric fields during the 10 May 2024 superstorm observed by ISRs over Sanya and Jicamarca. Geophys. Res. Lett. 52 (6). https://doi.org/10.1029/2024GL114543.